frontiers | Frontiers in Environmental Chemistry

TYPE Original Research
PUBLISHED 27 August 2024
DOI 10.3389/fenvc.2024.1447014

OPEN ACCESS

EDITED BY
Dipak Ashok Jadhav,
Korea Maritime and Ocean University, Republic of Korea

REVIEWED BY
Yihao Zhou,
University of California, Los Angeles, United States
Gunaseelan Kuppurangan,
University of Galway, Ireland

*CORRESPONDENCE
Mauricio Isaacs,
misaacs@uc.cl

RECEIVED 10 June 2024
ACCEPTED 05 August 2024
PUBLISHED 27 August 2024

CITATION
Gazzano V, Mardones-Herrera E, Sáez-Pizarro N, Armijo F, Martinez-Rojas F, Ruiz-León D, Honores J and Isaacs M (2024) Carbon dioxide electrochemical reduction by copper nanoparticles/ionic liquid-based catalytic inks.
Front. Environ. Chem. 5:1447014.
doi: 10.3389/fenvc.2024.1447014

Carbon dioxide electrochemical reduction by copper nanoparticles/ionic liquid-based catalytic inks

Valeria Gazzano[1,2], Elías Mardones-Herrera[1,2], Natalia Sáez-Pizarro[2], Francisco Armijo[1,2], Francisco Martinez-Rojas[1,2], Domingo Ruiz-León[3], Jessica Honores[1,2] and Mauricio Isaacs[1,2]*

[1]Departamento de Química Inorgánica, Facultad de Química y de Farmacia, Pontificia Universidad Católica de Chile, Santiago, Chile, [2]Millennium Institute on Green Ammonia as Energy Vector-MIGA, Pontificia Universidad Católica de Chile, Santiago, Chile, [3]Departamento de Química de Materiales, Facultad de Química y Biología, Universidad de Santiago de Chile, Santiago, Chile

The development of copper nanoparticle (CuNP)-based catalysts for the electrochemical reduction of carbon dioxide (ECO_2-R) offers a promising approach to enhance its transformation into other industrially significant compounds. This study reports ECO_2-R at −1.3 V vs RHE using CuNPs and catalytic inks composed of CuNPs and ionic liquids (ILs), observing significant differences in the selectivity of each catalyst. Specifically, CuNPs alone show a preference for producing ethylene and aqueous products, such as formic acid, ethanol, and formaldehyde. In contrast, the addition of ILs to the catalytic system redirects selectivity toward gaseous products, with methane being the main product. These findings highlight the potential to optimize catalyst composition to tailor the selectivity of CO_2 conversion processes. ILs modify the catalytic environment and influence reaction pathways, enabling the selection of specific products.

KEYWORDS

electrochemical CO_2 reduction, ionic liquids, copper nanoparticles, catalytic inks, CO_2 conversion

1 Introduction

The atmospheric carbon dioxide (CO_2) level has drawn the attention of the scientific community in recent years (Jones et al., 2017; Häder and Barnes, 2019; Alma et al., 2020; Dusenge et al., 2020; Leisner, 2020; Lv et al., 2020; Wu et al., 2020). There is a direct relationship between increasing CO_2 concentration and global temperatures (Shukla et al., 2017). Recent measurements of the CO_2 concentration in the atmosphere show the highest increase in the last 800 years (World Meteorological Organization (WMO), 2019; Yan et al., 2019), reaching values of approximately 426 ppm (National Oceanic and Atmospheric Administration (NOAA), n.d.). This estimates that the CO_2 level has quadrupled since 1960. The excessive elevation of atmospheric CO_2 levels is a global predicament that fosters the occurrence of the greenhouse effect, thereby contributing to the phenomenon of global warming. Despite the severe damage to both the environment and human beings caused by

climate change, it is predicted that fossil fuels will remain an important source of energy in the future. Additionally, human activities have released carbon sequestered by plants millions of years ago into the atmosphere. Therefore, it is crucial to develop carbon dioxide capture technologies to mitigate atmospheric CO_2 levels. Carbon dioxide capture is an effective way to reduce the concentration of this gas in the atmosphere, enabling its transformation into other industrially relevant species and, thus, closing the anthropogenic carbon cycle (Dreyse et al., 2015; Calfumán et al., 2017; Landaeta et al., 2018; 2020; Honores et al., 2019; Guzmán et al., 2020; Nguyen et al., 2020; Mardones-Herrera et al., 2022). One of the methods currently being explored for CO_2 conversion is electrochemical reduction using various catalysts (Handoko et al., 2018; Asadi et al., 2019; Jo et al., 2019; Low et al., 2019; Yue et al., 2019; Zhang et al., 2019; Zhou et al., 2019). However, due to the high formation enthalpy of CO_2 at standard temperature and pressure (298 K and $\Delta Hf = -393.5$ kJ/mol), identifying an appropriate electrocatalyst that can operate efficiently and selectively at low overpotentials while remaining economically viable presents a significant challenge in terms of sustainability and energy efficiency.

Copper is a transition metal that uniquely transforms carbon dioxide into species with two or more carbon atoms in their structure. The product distribution is influenced by both the local pH on the electrode surface and the crystallographic orientation of the copper nanoparticles (CuNPs). It is crucial to highlight that the key intermediate in hydrocarbon formation is the CO species, as widely recognized in the literature (Rutkowska et al., 2020; Wang et al., 2020). In addition, it is necessary to distinguish between the different pathways for different types of products to be obtained. Research using density functional theory (DFT) proposes that this distinction involves obtaining products with different numbers of carbon atoms in their structure (C1 and C2) (Kortlever et al., 2015). Another point to consider is the selectivity of copper structures toward carbon dioxide. The Cu(111) crystallographic orientation is selective for methane, while Cu(100) is selective for ethylene, and Cu(110) produces oxygenated products. For the C1 pathway, the CO intermediate species is first reduced to a formyl-type species (*CHO) or *COH, which is further reduced to methane. This mechanism assumes an early breaking of the second C-O bond, but Durand et al. (2011) proposed that a late breaking of this bond may be thermodynamically more favorable than the previously mentioned pathway. Conversely, if high overpotentials are used, it is possible to induce the dimerization of the CO intermediate species, resulting in the formation of ethylene. However, it should be noted that most of the ethylene produced occurs when the current density reaches values above 10 mA cm^{-2} and takes place in both the Cu(100) and Cu(111) crystallographic orientations (Montoya et al., 2013).

On the other hand, the key to the C2 pathway at low overpotentials is the dimerization of the CO intermediate species mediated by an electron transfer to form the $*C_2O_2^-$ intermediate. It should be noted that this process is the rate-determining step in the carbon dioxide reduction reaction via the C2 pathway, followed by a subsequent protonation of the negatively charged dimer (Calle-Vallejo and Koper, 2013; Montoya et al., 2015). DFT studies on these processes[28] showed that the intermediate produced by dimerization is more stable in square orientations formed by four atoms, explaining the selectivity toward ethylene formation by the Cu(100) facet at low potentials.

The formation of other reaction products, such as oxygenated products, is not entirely clear as the faradaic efficiencies associated with these are very low, and the reaction products can only be detected by very sensitive methods, such as nuclear magnetic resonance. However, the literature acknowledges that formate production follows a separate pathway from that of methane and ethylene formation as formate cannot be further reduced to other products (Cook et al., 1989; Hori et al., 1989).

Another critical aspect of the electrochemical reduction of carbon dioxide (ECO_2-R) mechanism is the local pH on the electrode surface. Increased buffering capacity results in higher selectivity for methane (Chen et al., 2015) due to decreased local pH, consistent with the results published by Koper et al., which indicates that methane production is directly related to proton activity (Kortlever et al., 2015). Conversely, low buffering capacity, or an alkaline pH environment, favors the dimerization of the CO intermediate to form ethylene. Alternatively, nanoparticulated materials show better activity toward CO_2 reduction due to an increased active surface area. Thus, copper nanoparticles are used as catalysts for CO_2 electrochemical reduction (Li X. et al., 2022; Li et al., 2022 G.; Castro-Castillo et al., 2022; Mardones-Herrera et al., 2022; Yang et al., 2023). However, copper nanoparticles face a significant drawback as they tend to rapidly oxidize (Isaacs et al., 2018) upon exposure to atmospheric oxygen and agglomerate. This limitation poses a significant challenge to their long-term use and must be addressed before they can be effectively used in various applications.

One approach to preventing the short-term oxidation of CuNPs is using them in conductive ink formulations. Copper-based inks comprise a colloidal dispersion of conductive nanoparticles (specifically, copper nanoparticles) in a dispersant medium serving as the continuous phase, a dispersant agent that imparts stability to the suspension by preventing agglomeration, and a binder that enhances adhesion of the ink to the underlying substrate (Tam et al., 2016). Moreover, conductive inks are widely used in oxygen reduction and oxygen evolution reactions (Polani et al., 2018; Costa Bassetto et al., 2019; Venezia et al., 2019), flexible electronics (Chen et al., 2021; Tian et al., 2021), solar cells (Li et al., 2021), and fuel cell applications (Gatard et al., 2021), but they are rarely used in electrochemical carbon dioxide reduction. The incorporation of copper nanoparticles into this system is anticipated to produce a novel and long-lasting material, preserving the electrocatalytic properties of the copper nanoparticles over an extended period. Nevertheless, conductive inks have different species in their composition, especially polymers, where their presence probably interferes with the electron transfer reaction between CuNPs and CO_2. To attempt to rectify this issue, some ionic liquids (ILs) have been incorporated into the ink composition due to their capability to increase the conductivity of flexible electronic devices (Chun et al., 2013), and they have been used for oxygen reduction reaction (ORRs) with this purpose (Snyder et al., 2010), so it is possible to apply this property for the systems of this work.

Imidazolium cation-based ILs were selected based on their extensively investigated interaction with CO_2 (Anthony et al.,

2002; 2005; Aki et al., 2004; Muldoon et al., 2007). The role of anions in ILs is the main factor in CO_2 absorption (Zeng et al., 2017). Anthony et al. (2005) studied the effect of different cations—imidazolium, ammonium, pyrrolidinium, and phosphonium—with the same anion and found that solubility is almost the same; on the other hand, Aki et al. (2004) and Muldoon et al. (2007) showed that CO_2 solubility in imidazolium-based ILs exhibited an increase in the following order of anions: $[NO_3^-]$ < [dca] < $[BF_4]$ < $[PF_6]$ < [OTf] < [TFSI] < [methide] (tris-(trifluoromethyl sulfonyl)methide) at 25°C. This study also demonstrates that the solubility of CO_2 occurs due to the interaction with the anion of the IL, but the mechanism by which this occurs is still unknown. Furthermore, it has been observed that ILs that feature fluorinated anions exhibit a greater affinity for CO_2 absorption than those with non-fluorinated anions. Additionally, the solubility of CO_2 within ILs is directly proportional to the number of fluorine substituents present in the anionic component (Baltus et al., 2004; Zhang et al., 2008; Jung et al., 2012; Pereiro et al., 2013). All these solubility properties enable them to be used as an electrolyte in the ECO_2-R processes (Barrosse-Antle and Compton, 2009; Rosen et al., 2011; Zhou et al., 2014; Lau et al., 2016; Feng et al., 2018; Ma et al., 2022), and they act as an electrocatalyst in those ECO_2-R processes (Quezada et al., 2014b; 2014a; Honores et al., 2017), decreasing the energy barriers of reactions by building complexes with the intermediates generated during the reaction (Maniam and Paul, 2021). In contrast, the concept of surface-confined ionic liquid layer (SCILL) provides a way to regulate catalytic activity and selectivity (Zhang and Etzold, 2021). Recently, this concept was applied in electrocatalysis, and it was shown to be a new and growing field where key applications have emerged in energy storage and conversion processes, such as hydrogen evolution (Zhang C. et al., 2023), oxygen evolution (Avid et al., 2022), and electrochemical reduction of carbon dioxide (Parada et al., 2022). ILs in SCILL systems can function in different ways: they can modify the concentration and/or local mass transport of reactants and/or intermediates at active sites due to differences in solubility and/or diffusion coefficients of these species compared to conventional solvents (Zhang C. et al., 2023). In addition, they can function as ligands on the surface by interacting directly with active sites, causing changes in the electronic structures of the surface. Additionally, ILs can selectively hinder unwanted surface sites by competing with them for adsorption, resulting in changes in product distribution. Furthermore, the steric properties of ILs can help stabilize copper nanoparticles (He and Alexandridis, 2015). Therefore, in addition to all the aforementioned characteristics, ILs are also valuable as components in catalytic inks.

The primary objective of the present study is to investigate the electrochemical reduction of carbon dioxide using CuNPs and catalytic inks composed of CuNPs and various ILs. The study aims to synthesize and characterize these materials, evaluate their electrocatalytic performance for CO_2 reduction, and compare the selectivity and efficiency of different IL formulations in directing the product distribution toward desired compounds, such as methane and ethylene. Additionally, the present work analyzes the interaction mechanisms between CuNPs, ILs, and CO_2 to understand how ILs influence the catalytic environment and reaction pathways. By achieving these objectives, the study seeks to optimize the composition of CuNP-based catalytic inks to enhance their selectivity and efficiency for industrially significant CO_2 conversion processes.

2 Materials and methods

2.1 Materials

Anhydrous ethylene glycol (EG) (99.8%), copper sulfate pentahydrate ($CuSO_4$•$5H_2O$), polyvinylpyrrolidone (PVP), M_w~40,000, sodium hypophosphite (NaH_2PO_2•H_2O), and phenol were purchased from Sigma-Aldrich; 1-butyl-3-methylimidazolium bis(trifluoromethylsulfonyl)imide, 1-butyl-3-methylimidazolium tetrafluoroborate, and 1-butyl-3-methylimidazolium trifluoromethanesulfonate ILs (Table 1) were purchased from IoLiTec and dried in vacuum at 70°C for 8 h; potassium bicarbonate ($KHCO_3$), ethanol, methanol, dimethyl sulfoxide (DMSO), 2-propanol, and deuterium oxide (D_2O) were purchased from Merck; argon, CO_2, and nitrogen were purchased from Indura; and the Nafion® 117 proton exchange membrane was purchased from Fuel Cell Store. Milli-Q water was obtained using a Heal Force Water Purification System. All chemicals except ILs were used without further purification and treatment.

2.2 Synthesis of copper nanoparticles, ink formulation, and electrode preparation

A previously reported procedure was used to prepare copper nanoparticles (Lee et al., 2008). First, 5.55 g of PVP and 19.45 mmol of sodium hypophosphite were dissolved in 15 mL of a 3:1 EG:methanol solution (SA). Then, 5.68 mmol of copper sulfate was dissolved in 5 mL of a 3:1 EG:methanol solution (SB). SB was introduced in a three-necked flask, and both solutions were saturated with argon for 30 min. SB was heated up to 90°C; then, SA was added drop by drop to the stirring system, and after approximately 10 min, the solution turned from green to henna, indicating the formation of copper nanoparticles. The reaction was quenched with chilled and nitrogen-saturated Milli-Q water. To separate the copper nanoparticles from the reaction system, the resulting suspension was centrifuged for 15 min at 10,000 rpm. Afterward, the copper nanoparticles were washed with chilled and nitrogen-saturated water and deaired ethanol. Finally, the copper nanoparticles were dried in a vacuum environment for 3 h at 110°C.

Catalysts were prepared by adding 20 mg of CuNPs to 1 g of isopropanol or 1 g of solution of PVP/IL/isopropanol, as shown in Table 2. Each catalyst was sonicated for 30 min before use. PVP was used to provide surface adhesion and avoid the agglomeration of CuNPs.

The electrodes used in electrochemical measurements were prepared by adding 5 µL of suspension (CuNPs or CuNP-IL ink) three times on a 3-mm-diameter glassy carbon disk, and for ECO_2-R, 20 µL of suspension was deposited three times on a 1-cm^2-surface area glassy carbon plate by spin coating at 100 rpm. For CuNP-IL inks, before use, the electrode was dried for 5 min at 60°C. On the other hand, each glassy carbon with a deposit of PVP/IL and CuNPs/PVP/IL ink is named as mentioned in Table 2.

When the catalysts are on a glassy carbon surface, the abbreviation "GC" is prefixed, for example, "GC/CuNPs."

TABLE 1 ILs evaluated in this study.

Ionic liquid	Chemical formula	Cation	Anion	Abbreviation	Reference
1-Butyl-3-methyl imidazolium bis(trifluoromethylsulfonyl)imide	$(C_{10}H_{15}F_6N_3O_4S_2)$	(C_4H_9) (CH_3) $(C_3N_2H_4H)^+$	$CF_3SO_2CF_3SO_2N^-$	[BMIm]TFSI	[78]
1-Butyl-3-methyl imidazolium tetrafluoroborate	$(C_8H_{15}F_4N_2B)$	(C_4H_9) (CH_3) $(C_3N_2H_4H)^+$	$[BF_4]^-$	$[BMIm]BF_4$	[78]
1-Butyl-3-methyl imidazolium trifluoromethane sulfonate	$(C_9H_{15}F_3N_2O_3S)$	(C_4H_9) (CH_3) $(C_3N_2H_4H)^+$	$[CF_3SO_3]^-$	[BMIm]OTf	[78]

TABLE 2 Nomenclature and composition of each catalyst.

Catalyst	Abbreviation	Q_{Isop}[a] (mL)	Q_{PVP}[b] (mg)	Q_{IL}[c] (μL)
Copper nanoparticles	CuNPs	1.27	0	0
PVP/$[BMIm]BF_4$	BF_4 ink	1.15	50	42
CuNPs/PVP/$[BMIm]BF_4$	CuNP–BF_4 ink	1.15	50	42
PVP/[BMIm]OTf	OTf ink	1.15	50	38
CuNPs/PVP/[BMIm]OTf	CuNP–OTf ink	1.15	50	38
PVP/[BMIm]TFSI	TFSI ink	1.15	50	35
CuNPs/PVP/[BMIm]TFSI	CuNP–TFSI ink	1.15	50	35

[a]Q_{Isop}: amount of isopropanol.
[b]Q_{PVP}: amount of PVPK-10.
[c]Q_{IL}: amount of IL.

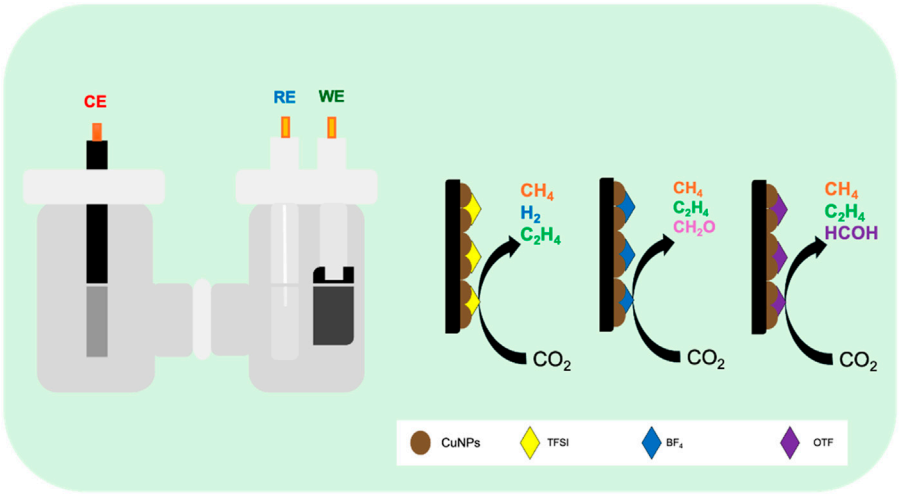

FIGURE 1
Electrochemical experimental setup.

2.3 Characterization of CuNPs and CuNP-IL inks

Copper nanoparticle morphology was determined by field emission scanning electron microscopy (FE-SEM) using an EDS detector. The crystallographic characterization was determined using an Bruker D8 Advance X-ray Diffractometer, Cu Kα, λ = 1.5406 Å, 40 KV, and 40 mA in the range of $5 < 2\Theta < 80$. The identification and crystallographic analysis were performed using CRYSFIRE suite software, and the crystallite size was determined using DIFFRAC.EVA 5.2 software. FT-IR spectroscopy was performed using an IR-ATR Spectrometer Thermo IS-10. UV–visible spectroscopy was performed using a Shimadzu MultiSpec-1510 Spectrophotometer.

Cyclic voltammetry (CV) and electrochemical impedance spectroscopy (EIS) measurements were carried out using a 760-B

CH Instrument with a glassy carbon disk electrode (0.071 cm^2) as the working electrode. CV analyses were carried out at 50 mV/s using an Ag/AgCl 3M reference electrode, with potentials converted to reversible hydrogen electrode (RHE) for clarity. EIS measurements were carried out at open-circuit potential (OCP) in the presence of argon and CO_2, with an amplitude of 10 mV and a frequency range of 10,000–0.001 Hz. ECO_2-R was carried out in an electrochemical cell (Figure 1) with a proton exchange membrane (Nafion® 117) at −1.3 V vs RHE for 3 h, using a 1-cm^2 glassy carbon plate and a multi-potentiostat (Ivium Technologies). Each electrochemical measurement was carried out in 0.1 M $KHCO_3$ as the supporting electrolyte, purged with argon or CO_2 for 30 min, with an Ag/AgCl 3M reference electrode and a platinum wire as the counter electrode.

2.4 Determination of products

Except for formaldehyde, water-soluble products were determined by nuclear magnetic resonance ^{1}H-NMR (400 MHz, Bruker) using a method previously reported by Kuhl et al. (2012), where calibration curves were fabricated with analytes of interest in a suitable range of concentration, with internal standards of phenol (50 mM) and DMSO (10 mM) in a 0.1 M $KHCO_3$ electrolyte. The water peak was suppressed in every collected spectrum. All samples were prepared using 700 µL of electrolyte with ECO_2-R products and 35 µL of the internal standard of phenol and DMSO in D_2O.

Formaldehyde was determined by UV–visible spectroscopy (Shimadzu MultiSpec-1510 with deuterium and tungsten lamps) through the chromotropic acid method. A calibration curve in the range 0.5–5 ppm was prepared using the following procedure: 500 uL of solution standard, 500 µL of chromotropic acid at 1%, and 4 mL of concentrated H_2SO_4 were mixed and heated up to 80oC–100°C. Then, 2 mL Milli-Q water was added, and 20 min later, the UV–visible measurements were performed at 575 nm.

Gas-phase products were quantified by gas chromatography (DANI Master GC) using a FID detector measuring hydrocarbons such as methane, ethane, ethylene, and propylene, and a µTCD detector was used to quantify the presence of hydrogen. For calibration curve construction, different volumes (10, 20, 30, 40, and 50 µL) of standard using a 50-µL Hamilton syringe were introduced to the GC. For methane quantification, DCG Refinery Gas Standard #1, CGA 170, mole, 5.2 L, 70 psi was used, and for hydrogen, Linde ultra-pure (99.999%) hydrogen was used as the standard. For electrolysis product quantification, 50 µL of the gas sample was measured. Calibration curves for methane and hydrogen are given in Supplementary Figure S1, S2.

3 Results and discussion

3.1 Characterization of CuNPs and CuNP–IL inks

The FE-SEM images of the (a) synthesized CuNPs; (b) CuNP–TFSI ink; (c) CuNP–OTf ink; and (d) CuNP–BF_4 ink are shown in Figure 2A. There is a granular morphology with some degree of agglomeration, which has a predominant size between 50 and 60 nm (Supplementary Figure S3A). Figures 2B,C, D display FE-SEM images for the catalytic inks, where the morphology of the nanoparticles has not changed and the size distribution is similar to CuNPs (Supplementary Figure S1B–D). Instead, it is possible to observe that when CuNPs are present in the ink formulation, the resulting image appears blurry. This is attributed to the addition of PVP and ILs, which, due to their high density and viscosity, impede the achievement of sharp images (Lu et al., 2019).

Energy-dispersive X-ray (EDX) spectroscopic images for CuNP–TFSI, CuNP–OTf, and CuNP–BF_4 inks, respectively, are displayed in Supplementary Figures S4–S7. For CuNP–TFSI and CuNP–OTf inks, fluorine and sulfur were observed due to the presence of TFSI and OTf anions, and for CuNP-BF_4 ink, fluorine from the BF_4 anion was detected. Furthermore, it is possible to note the presence of nitrogen in all ink spectra, which can be from the IL cation and PVP. Alternatively, Supplementary Figures S8–S10 display FE-SEM and EDX spectroscopy mapping images, revealing a uniform distribution of all components on the surface of the glassy carbon plate.

The X-ray diffraction pattern of the CuNPs shows that the main crystallographic orientation is Cu(111) (Figure 3) and presents characteristic peaks of cubic copper that were confirmed by index card JCPDS-ICDD, number 85–1,326, and is consistent with the previous report for this synthesis (Lee et al., 2008). The sample was indexed (R. Shirley, 2020) as a cubic cell in an Fm-3 space group with calculated cell parameter a = 3.6153 Å. The crystallite size was calculated using DIFFRAC.EVA 5.2 software, using the X-ray broadening of the (1 1 1), (2 0 0), and (2 2 0) diffraction peaks by the well-known Scherrer equation, $D = 0.9\,\lambda/B\cos\theta$, where D is the particle size in nm, λ is the wavelength of the X-ray (0.15405 nm for Cu–Ka), B is the corrected full-width at half-maximum, and θ is the diffraction angle. The calculated sizes were 43.3, 31.9, and 33.8 nm using CRYSFIRE suite software, which are of same magnitude and in good agreement order with the SEM analysis, and there is no detectable copper oxide. Calculations of the cell parameters and particle size details are given in Supplementary Figures S11, S12.

The UV–visible spectra of fresh (a) and 6-month-old (b) CuNPs and inks stored under atmospheric conditions are shown in Figure 4. The maximum absorption wavelength values are given in Table 3. For the fresh samples and aged inks, the UV–visible spectra exhibit a surface plasmon resonance characteristic of copper nanoparticles (Chan et al., 2007). However, a change in the CuNPs is notable as the maximum absorption shifted from 603 to 618 nm, and the shape of the spectrum also changed. In contrast, the ink spectra experienced minor shifts, with no significant changes in their overall shape. These results suggest that the ink formulation provides stabilization and protection to the CuNPs from oxidation and agglomeration (Tam et al., 2016).

3.2 Surface characterization through FT-IR spectroscopy

The FT-IR spectra of CuNP–BF_4 ink (Figure 5) and other catalysts are reported (Supplementary Figure S13). The FT-IR spectra for ILs (Johnston and Shriver, 1993; Schrader, 1996; Heimer et al., 2006; Holomb et al., 2008; Jeon et al., 2008; Noack

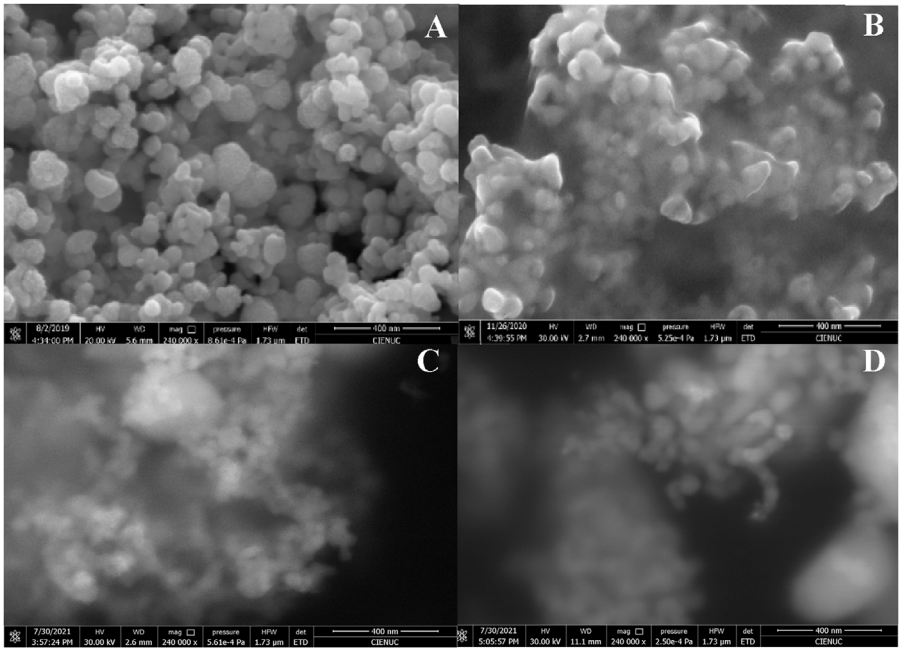

FIGURE 2
FE-SEM images of **(A)** CuNPs; **(B)** CuNP–TFSI ink; **(C)** CuNP–OTf ink; and **(D)** CuNP–BF4 ink.

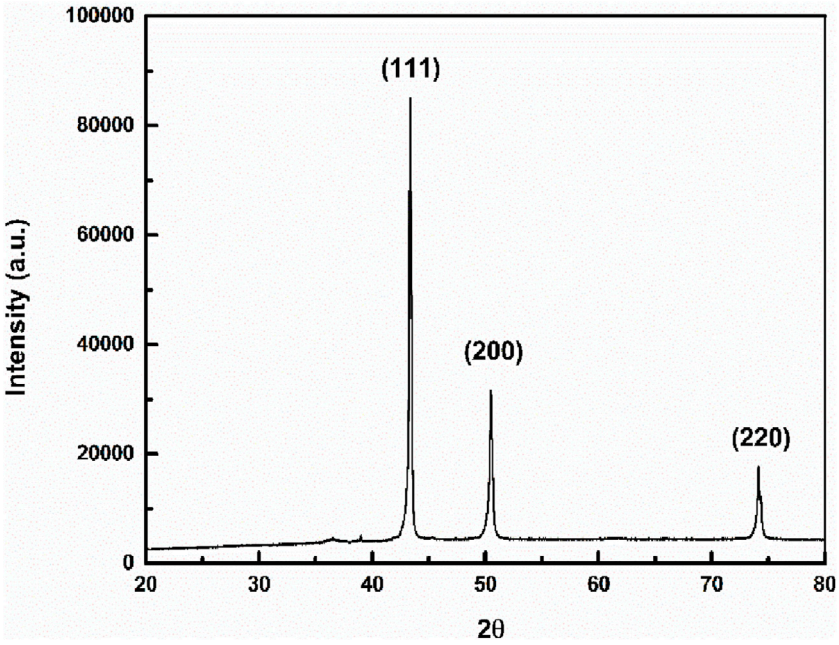

FIGURE 3
X-ray diffraction patterns of copper nanoparticles.

et al., 2010; Cha et al., 2014; Xu et al., 2017; Huang et al., 2018; Kausteklis et al., 2018; 2019) and PVP(Haaf et al., 1985; Lu et al., 2015; Shahi et al., 2017) are in good agreement with those in the literature, and in both images, two dotted lines were positioned at 3,521 cm^{-1} and 1,644 cm^{-1}, which correspond to polymeric OH^- and carbonyl bond from the PVP FT-IR spectra, respectively. Regarding the spectra obtained for the inks, some shifts were observed when compared with the spectra of the individual species, of which two stand out: the bathochromic shift in the vibration associated with the terminal polymeric OH^- and the hypsochromic shift in the band corresponding to the carbonyl bond from the PVP compound in each case. For the vibration associated with the OH^- bond, a

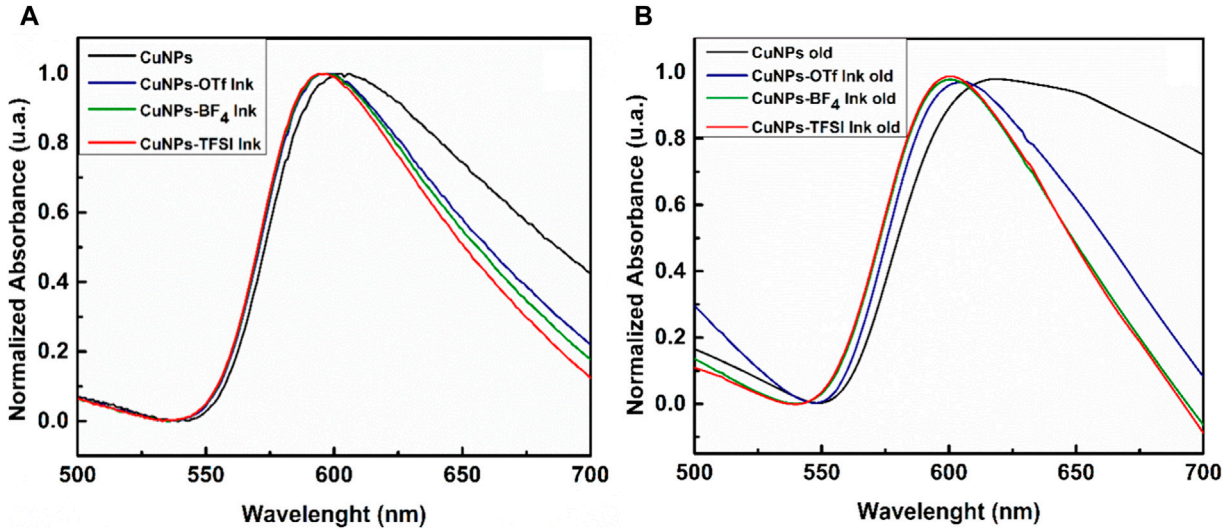

FIGURE 4
UV–visible spectroscopy for **(A)** fresh and **(B)** 6-month-old CuNPs and inks in deaired Milli-Q water.

TABLE 3 Maximum absorption wavelength for CuNPs and catalytic inks.

Sample	λ_{max} (nm)
CuNPs	603
CuNPs (old)	618
CuNP–OTf ink	597
CuNP–OTf ink (old)	606
CuNPs–BF_4 ink	597
CuNP–BF_4 ink (old)	600
CuNP–TFSI ink	595
CuNP–TFSI ink (old)	600

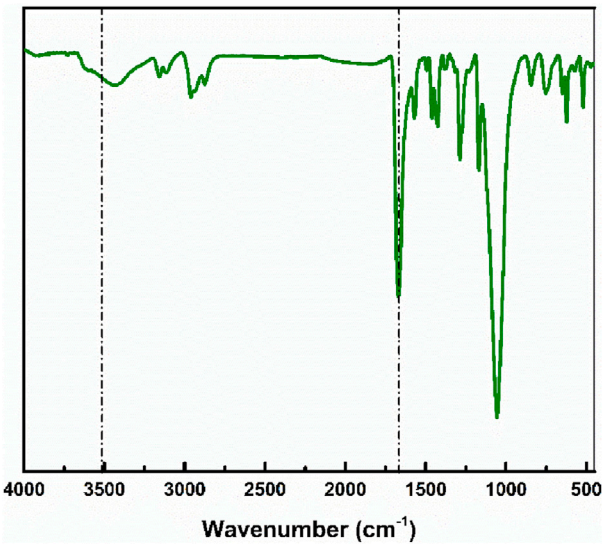

FIGURE 5
FT-IR spectra of CuNP–BF4 ink. The dotted lines correspond to the 3,521 and 1,644 cm^{-1} positions.

difference of 89 cm^{-1} was obtained for CuNP–TFSI ink and CuNP–BF_4 ink, and for CuNP–OTf ink, the shift corresponds to 48 cm^{-1}, while for the shifts in the carbonyl bond band, a difference of 31 cm^{-1} was obtained for CuNP–TFSI ink and 26 cm^{-1} for CuNP–BF_4 and CuNP–OTf inks.

The obtained values suggest that there may be an interaction between the CuNPs and the atoms associated with these bonds. It could also be expected that the ILs cause these changes in the bands, so the presence of each of these interactions in each case may also imply a difference in the surface environment.

3.3 Electrochemical measurements

3.3.1 Cyclic voltammetry

Cyclic voltammetry for GC/CuNPs and inks is shown in Figure 6 and S14–S16. In each one, there is a black cyclic voltammogram, which corresponds to the capacitive response of the blank electrode: the glassy carbon in the case of GC/CuNPs and GC/IL-PVP in the case of inks. In Supplementary Figure S14A, it is possible to observe two cathodic peaks at 0.33 and 0.5 V vs RHE and two anodic peaks at 0.76 and 1.0 V vs RHE in argon-saturated 0.1 $KHCO_3$ solution, corresponding to the reduction and oxidation processes of copper from GC/CuNPs, respectively. Meanwhile, cyclic voltammetry measurements for both GC/CuNP–OTf (Supplementary Figure S11A) and GC/CuNP–BF_4 (Figure 6A) inks showed only one oxidation and reduction process, and in GC/CuNP–TFSI ink, there are two oxidation peaks and one reduction peak. For CO_2-purged systems, there are also significant differences. In GC/CuNPs (Supplementary Figure S16B), there is only one peak for oxidation and another for reduction. Regarding copper-based inks, there is only one peak each for reduction and oxidation. Furthermore, there

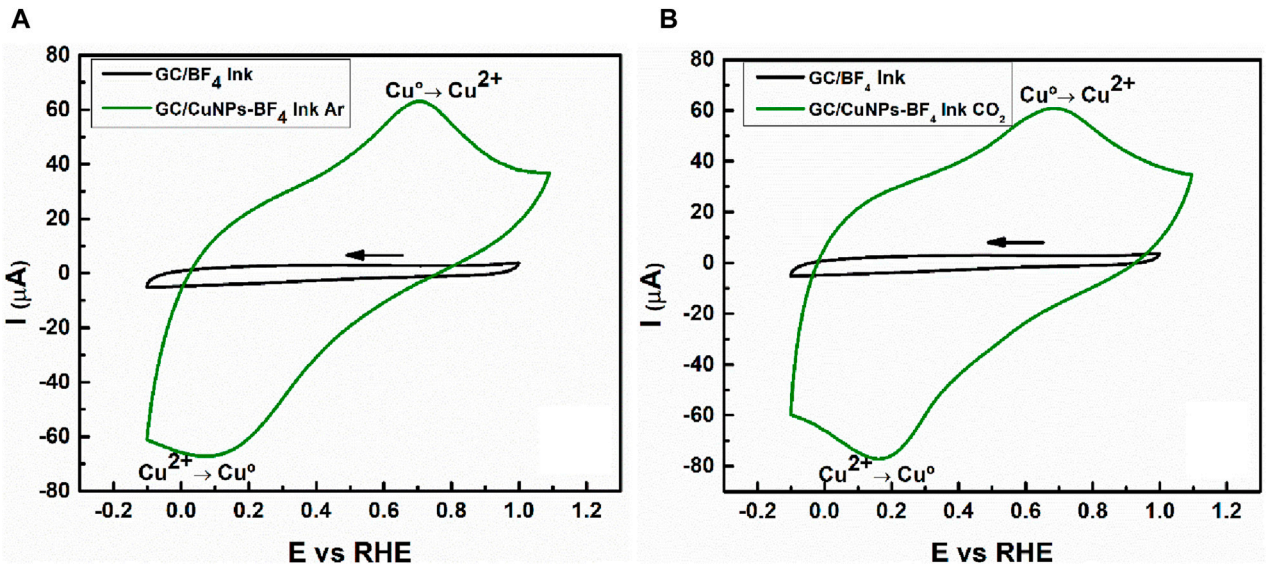

FIGURE 6
Cyclic voltammetry for GC/CuNP–BF_4 ink in 0.1 M $KHCO_3$ purged with argon **(A)** and CO_2 **(B)** at a scan rate of 50 mVs^{-1}. The blank measurements were performed with a modified glassy carbon electrode using the GC/BF_4 ink.

are important changes in the current intensity in each peak, for instance, CuNPs in Ar show a maximum value of −6 μA for the reduction peak and 8 μA for the oxidation peak. However, in CO_2, there is an increase to −210 and 240 μA. For CuNP-IL inks, lower current intensities were obtained than those of CuNPs alone. For CuNP–OTf and CuNP–TFSI inks, current intensities are lower than −15 and 15 μA for each peak in the Ar and CO_2 atmosphere, respectively, but for CuNP–BF_4, for both peaks in Ar and CO_2, current intensities of over −65 and 60 μA were observed (Figure 6). This phenomenon may be attributed to the GC/CuNP–BF_4 ink having a larger electroactive area, thus exhibiting higher conductivity. Nevertheless, GC/CuNP–TFSI ink exhibits a resistive behavior in the measurement in the CO_2 atmosphere compared to the measurement in argon and the other inks studied, suggesting that this modified electrode may be poorly conductive or possess a smaller electroactive surface area, or it could lead to hydrogen evolution reaction (HER) (Wang et al., 2021). On the other hand, CuNPs alone exhibit a higher intensity current when purged with CO_2. This can be attributed to the addition of new components, i.e., ILs, which work as chemical-trapping agents for CO_2 (Zhang et al., 2020). These differences are very significant because they suggest a change around the surface of GC/CuNP-IL (Castro-Castillo et al., 2022) inks compared to GC/CuNPs.

3.3.2 Linear sweep voltammetry

Linear sweep voltammetry (LSV) studies were performed in 0.1 M $KHCO_3$ in the presence of argon and carbon dioxide (Figures 7A,B) at a sweep rate of 5 $mV•s^{-1}$, using the OCP as the initial potential (Table 4). The onset potential for each is given in Table 5. In each case, there is a decrease in onset potential from Ar to CO_2-purged cells, which indicates that the required energy for ECO_2-R is less than that for HER. The three inks show similar behavior regarding the onset potential, but there is a difference in the current intensity; this behavior is consistent with the results from cyclic voltammetry, but in this case, the GC/CuNP–BF_4 ink is the catalyst with the higher current intensity. On the other hand, GC/CuNP-TFSI ink shows the lower current intensity for ECO_2-R of all the studied inks, and it is in good agreement with the literature due to the TFSI anion behavior (Cadena et al., 2004; Wang et al., 2021).

3.3.3 Electrochemical reduction of carbon dioxide

ECO_2-R was performed at −1.3 V vs RHE in 0.1 M $KHCO_3$ as the supporting electrolyte for 3 h. The product distribution results are given in Figure 8 and Supplementary Table S1. The Faradaic efficiency (FE) was calculated using Supplementary Equation 1 (Chen et al., 2015).

There were significant differences in product distribution between GC/CuNPs and each ink studied. For GC/CuNPs, the main product was ethylene, accounting for 41.9%. Nevertheless, lower FE for this product was obtained for the inks, with values of 12.9% for GC/CuNP–TFSI ink, 26.1% for CuNP–BF_4 ink, and 12.4% for GC/CuNP–OTf ink. It is reported in the literature that for the Cu(111) crystallographic orientation, methane should be the major product (Gattrell et al., 2006; Wang et al., 2023). However, methane formation is also dependent on the local pH, i.e., the activity of protons. In the case of GC/CuNPs, at this potential, the reaction leads to a basic local pH in the vicinity of the electrode, which favors the dimerization of the formyl intermediate, ultimately leading to the formation of ethylene[99]. In contrast, inks showed a major FE for methane compared to GC/CuNPs. GC/CuNP–TFSI, GC/CuNP–BF_4, and GC/CuNP–OTf inks showed methane as the main product with a 50.1%, 63.9%, and 38% FE, respectively, and for GC/CuNPs, the FE was only 9%. In the case of inks, an acidic environment provided by the ILs directs the reaction via the C1 pathway to produce methane (Cao et al., 2023). No carbon monoxide was detected in any of the studied electrolysis. Hydrogen was obtained in all electrolysis

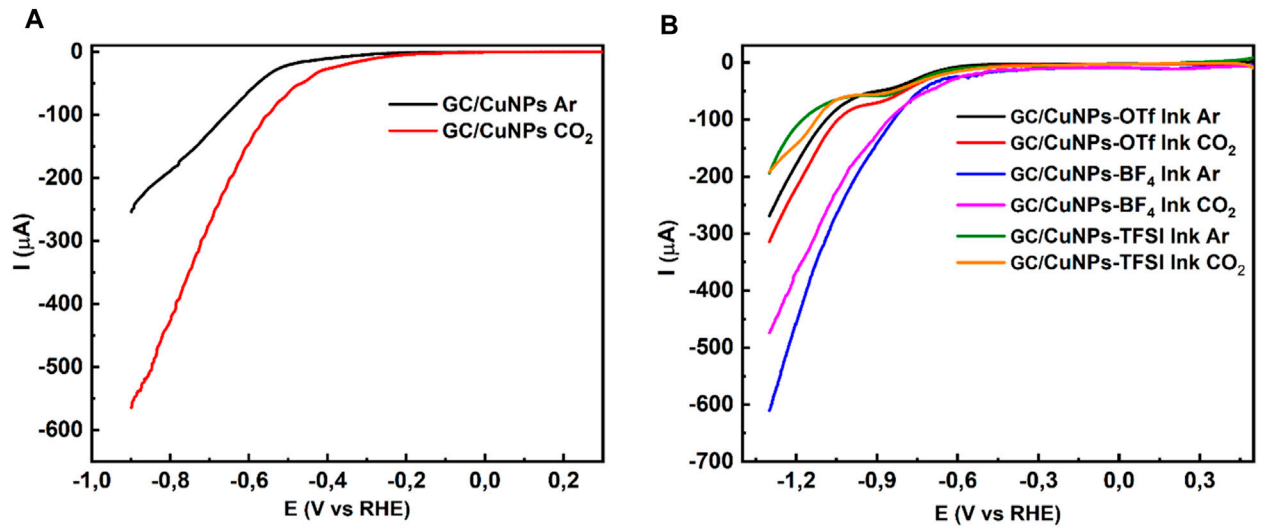

FIGURE 7
LSV for GC/CuNPs **(A)** and GC/CuNP–OTf ink, GC/CuNP–BF_4 ink, and GC/CuNP–TFSI ink **(B)** in the presence of argon and CO_2 with 0.1 M $KHCO_3$ as the supporting electrolyte at a scan rate of 5 mVs^{-1}.

TABLE 4 OCP values for each studied electrode in the presence of argon.

Electrode	OCP (V vs RHE)
GC/CuNPs	−0.351
GC/CuNP–TFSI ink	−0.532
GC/CuNP–OTf ink	−0.529
GC/CuNP–BF_4 ink	−0.553

[a]GC: glassy carbon.

TABLE 5 Onset potential vs RHE obtained from LSV measurements for each electrode.

Electrode	Ar E_{onset}	CO_2 E_{onset}
GC/CuNPs	−0.16	−0.11
GC/CuNP–BF_4 ink	−0.23	−0.16
GC/CuNP–OTf ink	−0.42	−0.09
GC/CuNP–TFSI ink	−0.46	−0.11

[a]GC: glassy carbon.

performed: for GC/CuNPs, an FE of 15% was obtained, while for GC/CuNP-TFSI ink, it was 30.1%. For GC/CuNP–OTf and CuNP–BF_4 inks, the FE for hydrogen was 7.2% and 5.4%, respectively.

3.3.4 Electrochemical impedance spectroscopy

Data were adjusted to an equivalent circuit shown in Figure 9 based on a previous reference (Martínez-Rojas et al., 2020). χ^2 values are 0.001 and 0.002, so the adjustment is representative in each analyzed system. The R1 value is the resistance of the solution, CPE1 is the double-layer capacitance, and R2 is the charge transfer resistance of the process. CPE2 is a capacitive element from the produced charges on the electrode surface, which increases with the addition of charged species such as ILs. CPE3 and R3 correspond to the double-layer components that describe the morphological irregularities of the electrode surface. When examining the data given in Table 6, it is possible to observe that the resistance of the solution (R1) shows the same behavior in all the studied systems, so the system is stable in each measurement. The charge transfer resistance (R2) for GC/CuNPs shows an increase from argon to carbon dioxide presence, but for GC/CuNP-BF_4 and GC/CuNP-OTf inks, the opposite effect occurs, i.e., R2 is higher in the presence of CO_2 than in argon, indicating a better performance in ECO_2-R.

On the other hand, the CPE3 component exhibits an increase in the GC/CuNP CO_2 compared to GC/CuNP Ar; meanwhile, for the other experiments, CPE3 retains the same magnitude order. This indicates that the stability in the ink systems is higher than that in GC/CuNPs, and the double layer decreases in function with the increase in stability.

The Nyquist plot for GC/CuNPs in the presence of Ar (red) and CO_2 (black) is displayed in Figure 10A. For the Ar-purged experiment, there is a capacitive response in the whole frequency range, and in the presence of CO_2, it is possible to observe the formation of a semicircle, indicating that CO_2 interacts with the CuNPs. In this case, the interaction occurs through adsorption, as it is at the OCP. In the case of the Bode plot (Figure 10B), a local accumulation of charge (Calfumán et al., 2017) takes place due to the formation of products, indicating the possible formation of an active site for GC/CuNPs in the presence and absence of CO_2, related to the relaxation time constants (Martínez-Rojas et al., 2020). In argon-purged measurements, there are two active sites, one at high frequencies and the other at low frequencies (2.2 ms and 85 s, respectively, [Table 7]), where different types of charge transfer can occur. On the other hand, in the presence of CO_2, a coupling of active sites can be observed, resulting in a shift toward intermediate frequencies. Relaxation time calculations were made using equation S2. These differences between both

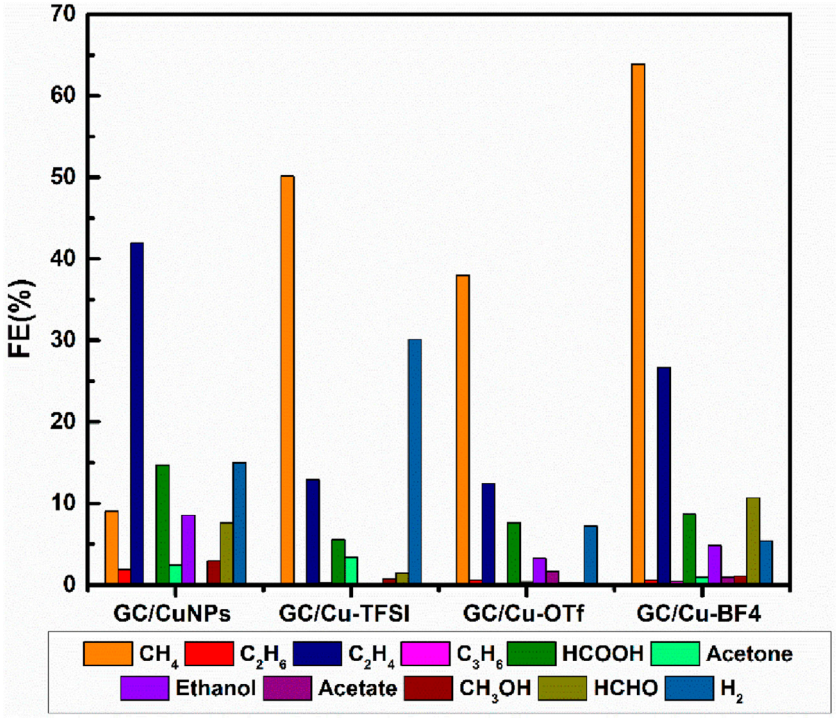

FIGURE 8
Faradaic efficiency for ECO_2-R for each reaction product at −1.3 V vs RHE.

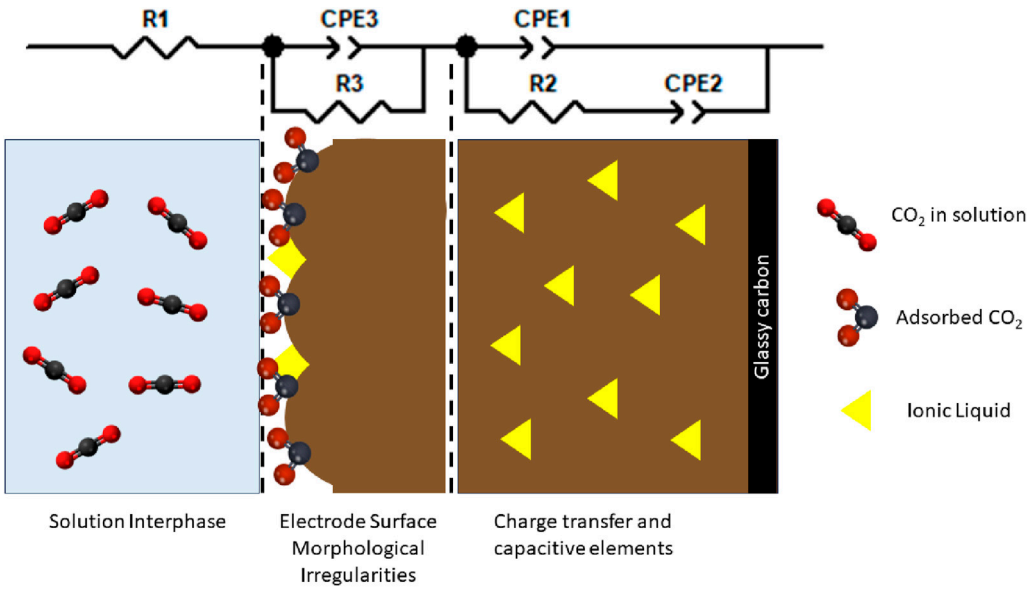

FIGURE 9
Equivalent circuit and diagram for studied systems.

experiments can be attributed to the morphological irregularities, the different crystallographic orientations in the CuNPs (Kas et al., 2015; Castro-Castillo et al., 2022; Mardones-Herrera et al., 2022), and their respective interactions with CO_2. In addition, a 45° phase angle was observed at low frequencies in the presence of CO_2, which means a diffusional behavior of carbon dioxide to the electrode surface.

The Nyquist and Bode plots for GC/CuNP–OTf and GC/CuNP–BF_4 inks show the same behavior (Figures 10C–F). A capacitive behavior is observed in the presence of argon in the

TABLE 6 Equivalent circuit elements from Figure 9 values for CuNPs and each studied ink.

Element	CuNPs/Ar	CuNPs/CO_2	CuNP–OTf ink/Ar	CuNP–OTf ink/CO_2	CuNP–BF_4 ink/Ar	CuNP–BF_4 ink/CO_2	CuNP–TFSI ink/Ar	CuNP–TFSI ink/CO_2
R1 (Ω)	183.8	211.8	170.0	165.1	180.9	186.1	175.5	174.9
CPE3-T (μF)	14	196.28	1.83	6.49	2.58	2.65	5.47	6.05
CPE3-P	0.69	0.78	0.86	0.76	0.87	0.84	1.09	0.79
R3 (Ω)	1,057	1880	3,661	1,069	3,491	2081	806.4	1,419
CPE1-T (μF)	61.1	166.02	7.1	65.8	8.39	59.78	1.58	56
CPE1-P	0.74	0.91	0.84	0.75	0.83	0.73	0.89	0.79
R2 (Ω)	6,725	15,033	16,133	4,715	22,661	6,009	ND[a]	3,932
CPE2-T (μF)	86.54	12.1	17.7	134.8	18.4	144.1	2.43	140.6
CPE2-P	0.86	0.28	0.69	0.83	0.72	0.80	0.33	0.86
χ^2	0.001	0.001	0.001	0.001	0.001	0.002	0.001	0.002

[a]ND: not determined.

Nyquist plot in both cases (Figures 10C,E), and for the CO_2-purged experiment, an increase in the capacitive response was observed, which means a decrease in the resistance to the charge transfer, indicating that the ink causes an increase in the interaction of CO_2 with the surface of the electrode. Bode plots (Figures 10D,F) exhibit the same behavior; the processes occur in the same regions, so the active sites are better defined than in CG/CuNPs, and there is a relevant decrease in the capacitance compared with CG/CuNPs in the presence of CO_2. These differences in active sites between the GC/CuNPs and inks could explain the product distribution in each case, where ethylene was the main product for GC/CuNPs and methane was the main product for GC/CuNP–BF_4 and GC/CuNP–OTf inks due to the formation of the active sites shown in each Bode plot.

On the other hand, the GC/CuNP–TFSI ink Nyquist plot (Figure 10G) shows a different behavior. The Nyquist plot shows a decrease in the capacitive response, which is in good agreement with the results obtained from cyclic voltammetry measurements. Furthermore, the Bode plot in the absence of CO_2 shows a wider frequency range than the other inks; thus, it is possible that there are more active sites for HER. This can be related to high faradaic efficiency for HER compared to the other experiments and can be due to the capacity of the [BMIm]TFSI to dissolve CO_2, which depends on the fluorinating degree of the anion (Cadena et al., 2004) and the nature of the TFSI anion that promotes HER (Wang et al., 2021).

However, the Bode plot for GC/CuNP–TFSI ink (Figure 10H) is very similar to that of the other inks, so the active sites should show the same behavior, but there is a main selectivity for methane and hydrogen (Figure 8); in contrast, in the other inks, there is a major selectivity for other C1 and C2 products. This can be related to two properties of this ionic liquid: the promotion of HER mentioned before, which explains the higher FE for the hydrogen obtained, and the other property is the hydrophobic nature of the [BMIm]TFSI IL. The hydrophobic surface promotes the increase in CO_2 and H^+ concentration in the electrode surface (Zhang Y. et al., 2023), which means that the ink should lead the C1 pathway to produce methane (Kortlever et al., 2015).

Based on the results obtained from the analysis of relaxation time constants, it can be inferred that there are different active sites for both CuNPs and inks, both in the presence of argon and carbon dioxide. On the other hand, the finding of these active sites and the product distribution obtained for each catalyst demonstrate that the inks have a SCILL behavior (Zhang and Etzold, 2021) due to the ILs promoting the suppression of certain products. For instance, in GC/CuNP-TFSI ink, the FE for ethylene is one of the lowest, and the FE for hydrogen is the highest. This is in good agreement with the SCILL study reported by Zhang et al. (2020), where IL molecules interact with one or more intermediates, leading to the production of the obtained species.

3.3.5 Proposed reaction mechanism

The following mechanism (Figure 11) is proposed based on published works (Nie et al., 2013; Kas et al., 2015). Gaseous CO_2 is adsorbed onto the surface of copper nanoparticles, which is the first necessary step for the reduction reaction to occur. Once adsorbed, the CO_2 molecule receives an electron, forming a radical anionic intermediate CO_2^-, stabilized by [BMIm]BF_4 (Ganesh, 2020; Li et al., 2023). The CO_2^- intermediate can receive another proton (H^+) and electron, converting into CO adsorbed on the copper surface.

The adsorbed CO can proceed through different pathways based on the catalyst configuration and reaction conditions. Differences in the intermediate steps of adsorption of CO_2 in the proposed mechanism are due to the interaction of the different crystallographic orientations of CuNPs (Kortlever et al., 2015). It is reported that Cu(111) leads to methane, Cu(100) to ethylene, and Cu(110) to oxygenated products. On the other hand, different ionic liquids stabilize intermediates in specific ways, influencing product formation. For example, BF_4^- stabilizes intermediates, favoring the production of methane (CH_4) and ethylene (C_2H_4).

3.3.6 Electrochemical stability of CuNPs and CuNP-IL inks

For the CuNPs, the initial current is more negative than −10 mA and stabilizes at approximately −20 mA after approximately 1 h, indicating significant catalytic activity and stable production of CO_2

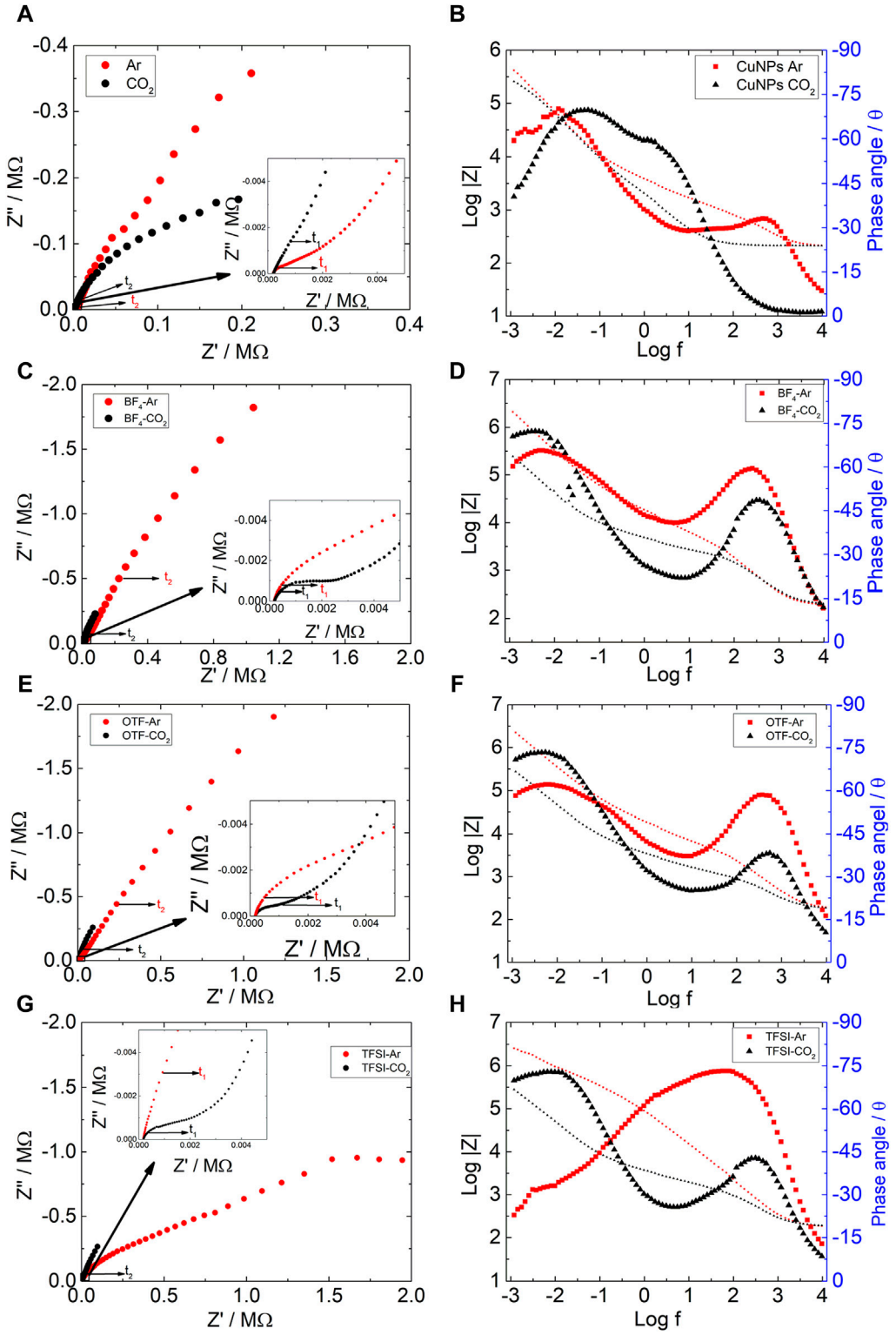

FIGURE 10
Nyquist diagram **(A,C,E,G)** and Bode plot **(B,D,F,H)** for GC/CuNPs, GC/CuNP–OTf, GC/CuNP–BF_4, and GC/CuNP–TFSI, respectively, in the presence of argon (red) and CO_2 (black). Dotted lines correspond to Log|Z| vs Log f, and square and triangle lines correspond to phase angle vs. Log **(F)**

reduction products over time. Copper nanoparticles can reduce CO_2 to various hydrocarbons, such as ethylene and methane, depending on the crystallographic orientation and local pH conditions (Kas et al., 2014).

For the GC/CuNP–BF_4 ink (Figure 12), the initial current is also more negative than −10 mA but stabilizes at approximately −10 mA, which is less negative compared to CuNPs without an ionic liquid. The presence of [BMIm]BF_4 appears to reduce the catalytic activity

TABLE 7 Relaxation time constants of each studied electrode.

Electrode	t_1 (ms)	t_2 (s)
CuNP Ar	2.2	85
CuNP CO_2	690	22
CuNP–OTf Ar	2.69	151.4
CuNP–OTf CO_2	3.24	181.9
CuNP–BF_4 Ar	3.94	182
CuNP–BF_4 CO_2	2.56	267
CuNP–TFSI Ar	14	--
CuNP–TFSI CO_2	3.24	123

of the CuNPs. According to the literature, BF_4^- stabilizes certain intermediates that favor methane and ethylene production, reducing the overall observed current. It has been reported that [BMIm]BF_4 produces significant amounts of methane and ethylene during the electrochemical reduction of CO_2 (Lau et al., 2016). For the GC/CuNP-OTf ink, the initial current mirrors that of other systems but stabilizes at approximately −15 mA. GC/CuNP–OTf ink seems to have an intermediate stabilizing effect on the catalytic activity of the CuNPs, likely through interactions with CO_2 reduction intermediates. This suggests that GC/CuNP–OTf ink may promote the formation of products like CO and formate, maintaining the electrode surface to be more active (Feng et al., 2018). In the case of GC/CuNP–TFSI ink, the initial current starts similar to GC/CuNP–BF_4 ink but stabilizes at approximately −10 mA. GC/CuNP–TFSI ink may act similarly to GC/CuNP-BF_4 ink by stabilizing certain intermediates and reducing the overall catalytic activity while favoring specific product formation. [BMIm]TFSI is known for its thermal and electrochemical stability (Feng et al., 2018). These results suggest that the ionic liquids [BMIm]BF_4, [BMIm]OTf, and [BMIm]TFSI significantly impact catalytic activity and product selectivity. We successfully achieved the electrochemical reduction of CO_2 using copper nanoparticles. The choice of ionic liquid influences the stabilization of reactive intermediates and the overall process efficiency, allowing for the tailoring of different hydrocarbon products as needed.

On the other hand, the performance of 6-month-old inks was similar to that of fresh ink obtained (Figure 13). Methane remains the main product of each ink, and the FE increased in the case of CuNP–OTf ink. Ethylene FE has similar value ranges, decreasing in

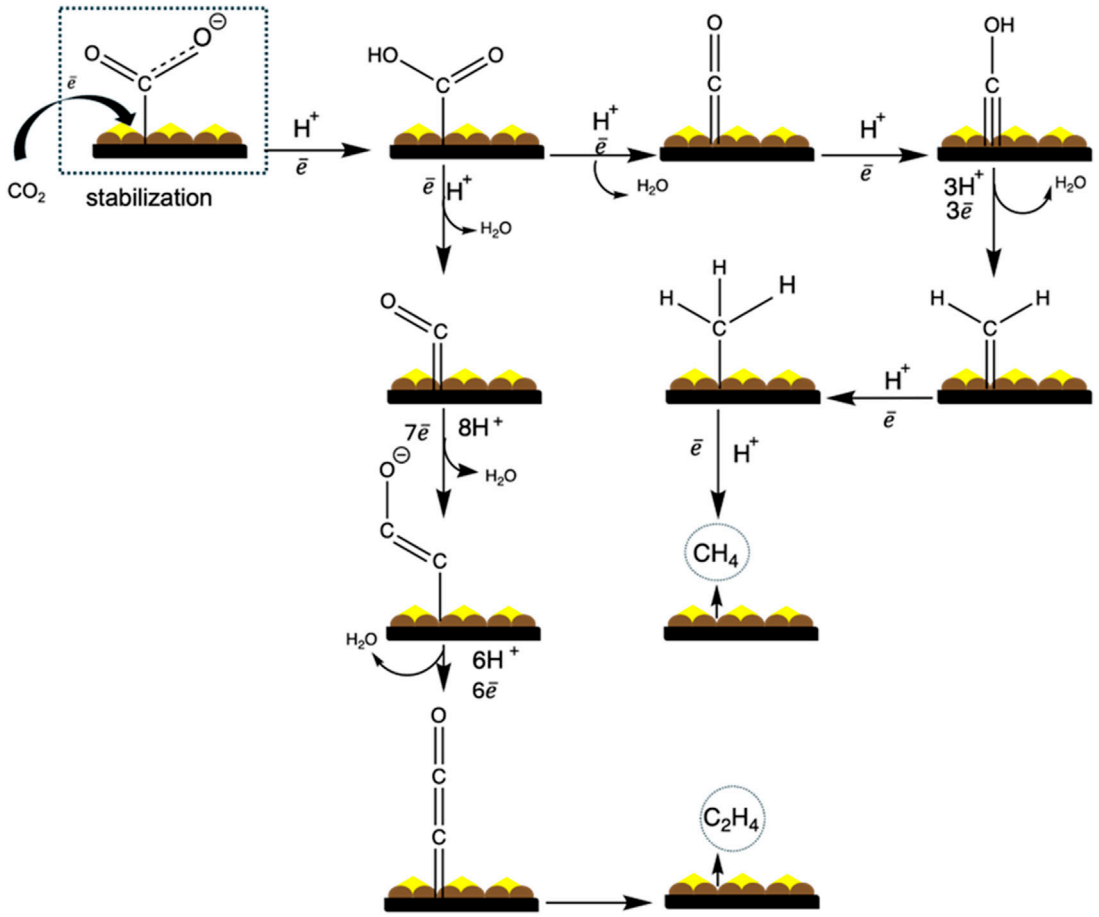

FIGURE 11
Proposed reaction mechanism for ECO_2-R.

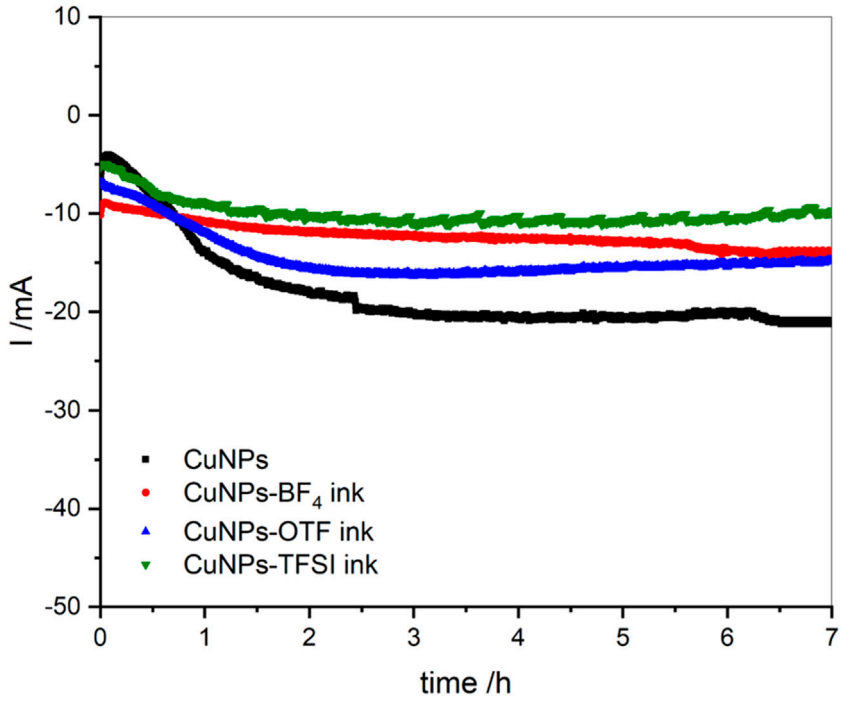

FIGURE 12
Electrolysis of GC/CuNPs (black), GC/CuNP–BF_4 ink (red), GC/CuNP–OTf (blue), and GC/CuNP–TFSI ink (green) at a controlled potential of –1.3 V vs RHE, saturated in CO_2 (pH 6.8). The current (I) is recorded as a function of time (t) over 7 h to determine the stability.

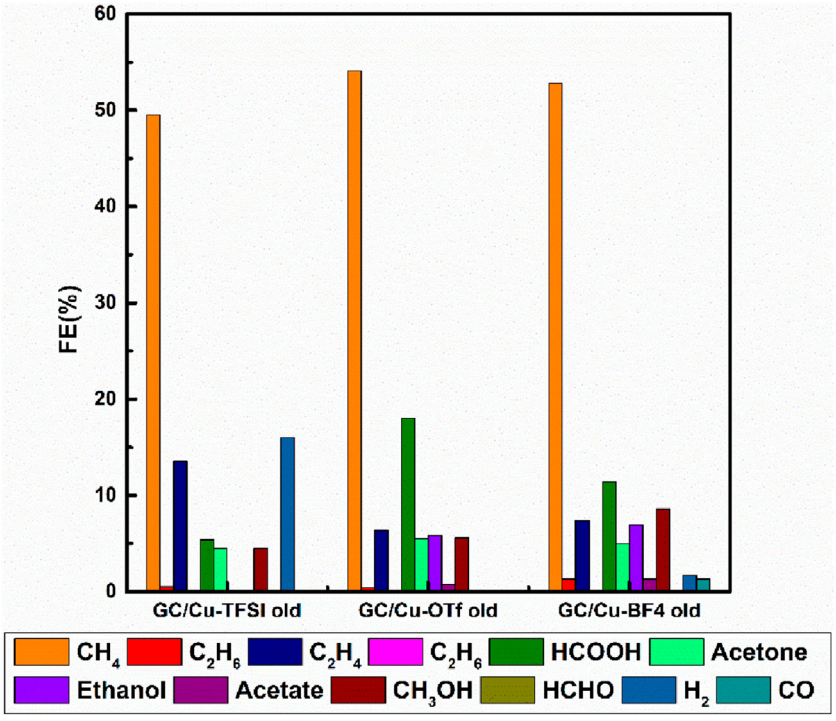

FIGURE 13
Faradaic efficiency for ECO_2-R for each reaction product at –1.3 V vs RHE with 6-month-old CuNP–IL inks.

the case of 6-month-old CuNP–BF4 ink. The FEs of formic acid, ethanol, and acetone are also similar across all the compared catalysts. These results suggest that despite the aging of the CuNP–IL inks, some products maintain stable efficiency. Despite some differences found, it can be inferred that the inks remain stable over a period of 6 months.

4 Conclusion

In this study, copper nanoparticles were synthesized using the wet chemical reduction method, resulting in a granular morphology with Cu(111) as the predominant crystallographic orientation. No copper oxides were detected, and copper-based inks exhibited a morphology and size distribution similar to CuNPs. Electrochemical reduction of carbon dioxide at −1.3 V vs RHE was performed using GC/CuNPs and GC/CuNP–IL-based inks. Significant differences in product distribution were observed, with ethylene and formic acid being the primary products for GC/CuNPs, while methane was obtained in varying proportions for GC/CuNP-IL inks despite the expected production of ethylene under the reaction conditions. Hydrogen was consistently generated in each electrolysis, particularly in the GC/CuNPs and GC/CuNP-TFSI ink systems. EIS analyses supported these findings, showing different active sites in Bode plots that could influence the concentration or local mass transport of reactants or intermediates in each ink system studied. The observed behavior of a surface-confined ionic liquid layer (SCILL) in the electrodes was attributed to changes in product distribution resulting from the addition of different ILs. Specifically, while the C2 mechanism was favored in GC/CuNPs, leading to ethylene formation, the C1 pathway predominated in GC/CuNP–TFSI, GC/CuNP–BF_4, and GC/CuNP–OTf inks, resulting in methane formation. Furthermore, GC/CuNP–TFSI inks exhibited high faradaic efficiency for hydrogen production, consistent with the nature of the TFSI anion.

Data availability statement

The raw data supporting the conclusion of this article will be made available by the authors, without undue reservation.

Author contributions

VG: writing–original draft, conceptualization, and methodology. EM: formal analysis, methodology, and writing–original draft. NS: methodology, writing–original draft, and formal analysis. FA: writing–review and editing. FM-R: formal analysis and writing–review and editing. DR: formal analysis and writing–original draft. JH: writing–review and editing and conceptualization. MI: writing–original draft, writing–review and editing, and funding acquisition.

Funding

The author(s) declare that financial support was received for the research, authorship, and/or publication of this article. This research work was financially supported by Funding Program 045–2019-FONDECYT-BM-INC.INV. (PROCIENCIA) assigned to the project “Manufactura Avanzada Incorporada En Dispositivos Recargables Ion-Litio Empleando Nuevos Materiales Basados En Liquidos Ionicos.”

Acknowledgments

The authors acknowledge FONDECYT Regular Projects 1181126, 1211518, and 1221179, FONDEQUIP EQM150020, EQM190016 and EQM150101, Millennium Institute of Green ammonia ICN 2021_023, and the ANID doctoral fellowship 21170164.

Conflict of interest

The authors declare that the research was conducted in the absence of any commercial or financial relationships that could be construed as a potential conflict of interest.

Publisher’s note

Supplementary material

The Supplementary Material for this article can be found online at: https://www.frontiersin.org/articles/10.3389/fenvc.2024.1447014/full#supplementary-material

References

Aki, S. N. V. K., Mellein, B. R., Saurer, E. M., and Brennecke, J. F. (2004). High-pressure phase behavior of carbon dioxide with imidazolium-based ionic liquids. *J. Phys. Chem. B* 108, 20355–20365. doi:10.1021/jp046895+

Alma, L., Kram, K. E., Holtgrieve, G. W., Barbarino, A., Fiamengo, C. J., and Padilla-Gamiño, J. L. (2020). Ocean acidification and warming effects on the physiology, skeletal properties, and microbiome of the purple-hinge rock scallop. *Comp. Biochem. Physiol. A Mol. Integr. Physiol.* 240, 110579. doi:10.1016/j.cbpa.2019.110579

Anthony, J. L., Anderson, J. L., Maginn, E. J., and Brennecke, J. F. (2005). Anion effects on gas solubility in ionic liquids. *J. Phys. Chem. B* 109, 6366–6374. doi:10.1021/jp046404l

Anthony, J. L., Maginn, E. J., and Brennecke, J. F. (2002). Solubilities and thermodynamic properties of gases in the ionic liquid 1-n-butyl-3-methylimidazolium hexafluorophosphate. *J. Phys. Chem. B* 106, 7315–7320. doi:10.1021/jp020631a

Asadi, M., Motevaselian, M. H., Moradzadeh, A., Majidi, L., Esmaeilirad, M., Sun, T. V., et al. (2019). Highly efficient solar-driven carbon dioxide reduction on molybdenum disulfide catalyst using choline chloride-based electrolyte. *Adv. Energy Mater* 9, 1–8. doi:10.1002/aenm.201803536

Avid, A., Ochoa, J. L., Huang, Y., Liu, Y., Atanassov, P., and Zenyuk, I. V. (2022). Revealing the role of ionic liquids in promoting fuel cell catalysts reactivity and durability. *Nat. Commun.* 13, 6349. doi:10.1038/s41467-022-33895-5

Baltus, R. E., Culbertson, B. H., Dai, S., Luo, H., and DePaoli, D. W. (2004). Low-pressure solubility of carbon dioxide in room-temperature ionic liquids measured with a quartz crystal microbalance. *J. Phys. Chem. B* 108, 721–727. doi:10.1021/jp036051a

Barrosse-Antle, L. E., and Compton, R. G. (2009). Reduction of carbon dioxide in 1-butyl-3-methylimidazolium acetate. *Chem. Commun.* 7, 3744–3746. doi:10.1039/b906320j

Cadena, C., Anthony, J. L., Shah, J. K., Morrow, T. I., Brennecke, J. F., and Maginn, E. J. (2004). Why is CO2 so soluble in imidazolium-based ionic liquids? *J. Am. Chem. Soc.* 126, 5300–5308. doi:10.1021/ja039615x

Calfumán, K., Honores, J., Guzmán, D., Ohlbaum, M., Armijo, F., Del Río, R., et al. (2017). Electrochemical conversion of carbon dioxide into CHO-containing compounds on multimetallic porphyrins. *ChemElectroChem* 4, 3314–3321. doi:10.1002/celc.201700653

Calle-Vallejo, F., and Koper, M. T. M. (2013). Theoretical considerations on the electroreduction of CO to C2 Species on Cu(100) electrodes. *Angew. Chem. - Int. Ed.* 52, 7282–7285. doi:10.1002/anie.201301470

Cao, Y., Chen, Z., Li, P., Ozden, A., Ou, P., Ni, W., et al. (2023). Surface hydroxide promotes CO2 electrolysis to ethylene in acidic conditions. *Nat. Commun.* 14, 2387. doi:10.1038/s41467-023-37898-8

Castro-Castillo, C., Nanda, K. K., Mardones-Herrera, E., Gazzano, V., Ruiz-León, D., Aguirre, M. J., et al. (2022). Growth direction and exposed facets of Cu/Cu2O nanostructures affect product selectivity in CO2 electroreduction. *Mater Chem. Phys.* 278, 125650. doi:10.1016/j.matchemphys.2021.125650

Cha, S., Ao, M., Sung, W., Moon, B., Ahlström, B., Johansson, P., et al. (2014). Structures of ionic liquid-water mixtures investigated by IR and NMR spectroscopy. *Phys. Chem. Chem. Phys.* 16, 9591–9601. doi:10.1039/c4cp00589a

Chan, G. H., Zhao, J., Hicks, E. M., Schatz, G. C., and Van Duyne, R. P. (2007). Plasmonic properties of copper nanoparticles fabricated by nanosphere lithography. *Nano Lett.* 7, 1947–1952. doi:10.1021/nl070648a

Chen, C. S., Handoko, A. D., Wan, J. H., Ma, L., Ren, D., and Yeo, B. S. (2015). Stable and selective electrochemical reduction of carbon dioxide to ethylene on copper mesocrystals. *Catal. Sci. Technol.* 5, 161–168. doi:10.1039/c4cy00906a

Chen, D., Kang, Z., and Li, W. (2021). Thin Ag films adhesive onto flexible substrates with excellent properties for multi-application. *J. Appl. Polym. Sci.* 138, 1–8. doi:10.1002/app.49806

Chun, K. Y., Kim, S. H., Shin, M. K., Kim, Y. T., Spinks, G. M., Aliev, A. E., et al. (2013). Free-standing nanocomposites with high conductivity and extensibility. *Nanotechnology* 24, 165401. doi:10.1088/0957-4484/24/16/165401

Cook, R., MacDuff, R., and Sammells, A. (1989). Evidence for formaldehyde, formic acid, and acetaldehyde as possible intermediates during electrochemical carbon dioxide reduction at copper. *Electrochem. Soc.* 136, 1982–1984. doi:10.1149/1.2097110

Costa Bassetto, V., Mensi, M., Oveisi, E., Girault, H. H., and Lesch, A. (2019). Print-light-synthesis of Ni and NiFe-nanoscale catalysts for oxygen evolution. *ACS Appl. Energy Mater* 2, 6322–6331. doi:10.1021/acsaem.9b00957

Dreyse, P., Honores, J., Quezada, D., and Isaacs, M. (2015). Electrocatalytic transformation of carbon dioxide into low carbon compounds on conducting polymers derived from multimetallic porphyrins. *ChemSusChem* 8, 3897–3904. doi:10.1002/cssc.201500816

Durand, W. J., Peterson, A. A., Studt, F., Abild-Pedersen, F., and Nørskov, J. K. (2011). Structure effects on the energetics of the electrochemical reduction of CO2 by copper surfaces. *Surf. Sci.* 605, 1354–1359. doi:10.1016/j.susc.2011.04.028

Dusenge, M. E., Madhavji, S., and Way, D. A. (2020). Contrasting acclimation responses to elevated CO2 and warming between an evergreen and a deciduous boreal conifer. *Glob. Chang. Biol.* 26, 3639–3657. doi:10.1111/gcb.15084

Feng, J., Zeng, S., Feng, J., Dong, H., and Zhang, X. (2018). CO2 electroreduction in ionic liquids: a review. *Chin. J. Chem.* 36, 961–970. doi:10.1002/cjoc.201800252

Ganesh, I. (2020). BMIM-BF4 RTIL: synthesis, characterization and performance evaluation for electrochemical CO2 reduction to CO over Sn and MoSi2 cathodes. *C (Basel)* 6, 47. doi:10.3390/c6030047

Gatard, V., De Masi, D., Chattot, R., Marin, I. M., Revert, J. M. A., Fazzini, P. F., et al. (2021). FeNi3 and Ni-based nanoparticles as electrocatalysts for magnetically enhanced alkaline water electrolysis. *Electrocatalysis* 11, 567–577. doi:10.1007/s12678-020-00616-9

Gattrell, M., Gupta, N., and Co, A. (2006). A review of the aqueous electrochemical reduction of CO2 to hydrocarbons at copper. *J. Electroanal. Chem.* 594, 1–19. doi:10.1016/j.jelechem.2006.05.013

Guzmán, D., Isaacs, M., Tsukuda, T., Yamazoe, S., Takahata, R., Schrebler, R., et al. (2020). CdTe quantum dots modified electrodes ITO-(Polycation/QDs) for carbon dioxide reduction to methanol. *Appl. Surf. Sci.* 509, 145386. doi:10.1016/j.apsusc.2020.145386

Haaf, F., Sanner, A., and Straub, F. (1985). Polymers of N-vinylpyrrolidone: synthesis, characterization and uses. *Polym. J.* 17, 143–152. doi:10.1295/polymj.17.143

Häder, D. P., and Barnes, P. W. (2019). Comparing the impacts of climate change on the responses and linkages between terrestrial and aquatic ecosystems. *Sci. Total Environ.* 682, 239–246. doi:10.1016/j.scitotenv.2019.05.024

Handoko, A. D., Wei, F., Jenndy, Yeo, B. S., and Seh, Z. W. (2018). Understanding heterogeneous electrocatalytic carbon dioxide reduction through operando techniques. *Nat. Catal.* 1, 922–934. doi:10.1038/s41929-018-0182-6

He, Z., and Alexandridis, P. (2015). Nanoparticles in ionic liquids: interactions and organization. *Phys. Chem. Chem. Phys.* 17, 18238–18261. doi:10.1039/c5cp01620g

Heimer, N. E., Del Sesto, R. E., Meng, Z., Wilkes, J. S., and Carper, W. R. (2006). Vibrational spectra of imidazolium tetrafluoroborate ionic liquids. *J. Mol. Liq.* 124, 84–95. doi:10.1016/j.molliq.2005.08.004

Holomb, R., Martinelli, A., Albinsson, I., Lassègues, J. C., Johansson, P., and Jacobsson, P. (2008). Ionic Liquid structure: the conformational isomerism in 1-butyl-3-methyl-imidazolium tetrafluoroborate ([bmim] [BF4]). *J. Raman Spectrosc.* 39, 793–805. doi:10.1002/jrs.1912

Honores, J., Quezada, D., Chacón, G., Martínez-Ferraté, O., and Isaacs, M. (2019). Synthesis of cyclic carbonates from CO2 and epoxide catalyzed by Co, Ni and Cu complexes in ionic liquids. *Catal. Lett.* 149, 1825–1832. doi:10.1007/s10562-019-02728-4

Honores, J., Quezada, D., García, M., Calfumán, K., Muena, J. P., Aguirre, M. J., et al. (2017). Carbon neutral electrochemical conversion of carbon dioxide mediated by [M: N +(cyclam)Cln] (M = Ni2+ and Co3+) on mercury free electrodes and ionic liquids as reaction media. *Green Chem.* 19, 1155–1162. doi:10.1039/c6gc02599d

Hori, Y., Kikuchi, K., Murata, A., Suzuki, S., and Takahashi, R. (1989). Formation of hydrocarbons in the electrochemical reduction of carbon dioxide at a copper electrode in aqueous solution. *J. Chem. Soc. Faraday Trans. 1 Phys. Chem. Condens. Phases* 85, 2309. doi:10.1039/f19898502309

Huang, T., Yan, P., Xu, Z., Liu, X., Xin, Q., Liu, H., et al. (2018). Structural dependence and spectroscopic evidence of methane dissolution in ionic liquids. *J. Phys. Chem. B* 122, 6007–6016. doi:10.1021/acs.jpcb.8b03178

Isaacs, M., Honores, J., and Quezada, D. (2018). "Carbon dioxide electrochemical reduction on tin and copper electrodes," in *Encyclopedia of interfacial chemistry: surface science and electrochemistry* (Elsevier), 401–411. doi:10.1016/B978-0-12-409547-2.13350-5

Jeon, Y., Sung, J., Seo, C., Lim, H., Cheong, H., Kang, M., et al. (2008). Structures of ionic liquids with different anions studied by infrared vibration spectroscopy. *J. Phys. Chem. B* 112, 4735–4740. doi:10.1021/jp7120752

Jo, W. K., Kumar, S., and Tonda, S. (2019). N-doped C dot/CoAl-layered double hydroxide/g-C3N4 hybrid composites for efficient and selective solar-driven conversion of CO2 into CH4. *Compos B Eng.* 176, 107212. doi:10.1016/j.compositesb.2019.107212

Johnston, D. H., and Shriver, D. F. (1993). Vibrational study of the trifluoromethanesulfonate anion: unambiguous assignment of the asymmetric stretching modes. *Inorg. Chem.* 32, 1045–1047. doi:10.1021/ic00058a050

Jones, E. M., Fenton, M., Meredith, M. P., Clargo, N. M., Ossebaar, S., Ducklow, H. W., et al. (2017). Ocean acidification and calcium carbonate saturation states in the coastal zone of the West Antarctic Peninsula. *Deep Sea Res. 2 Top. Stud. Oceanogr.* 139, 181–194. doi:10.1016/j.dsr2.2017.01.007

Jung, Y. H., Jung, J. Y., Jin, Y. R., Lee, B. C., Baek, I. H., and Kim, S. H. (2012). Solubility of carbon dioxide in imidazolium-based ionic liquids with a methanesulfonate anion. *J. Chem. Eng. Data* 57, 3321–3329. doi:10.1021/je3001377

Kas, R., Kortlever, R., Milbrat, A., Koper, M. T. M., Mul, G., and Baltrusaitis, J. (2014). Electrochemical CO2 reduction on Cu2O-derived copper nanoparticles: controlling the catalytic selectivity of hydrocarbons. *Phys. Chem. Chem. Phys.* 16, 12194–12201. doi:10.1039/C4CP01520G

Kas, R., Kortlever, R., Yilmaz, H., Koper, M. T. M., and Mul, G. (2015). Manipulating the hydrocarbon selectivity of copper nanoparticles in CO2 electroreduction by process conditions. *ChemElectroChem* 2, 354–358. doi:10.1002/celc.201402373

Kausteklis, J., Aleksa, V., Iramain, M. A., and Brandán, S. A. (2018). Effect of cation-anion interactions on the structural and vibrational properties of 1-buthyl-3-methyl imidazolium nitrate ionic liquid. *J. Mol. Struct.* 1164, 563–576. doi:10.1016/j.molstruc.2018.03.100

Kausteklis, J., Aleksa, V., Iramain, M. A., and Brandán, S. A. (2019). DFT and vibrational spectroscopy study of 1-butyl-3-methylimidazolium trifluoromethanesulfonate ionic liquid. *J. Mol. Struct.* 1175, 663–676. doi:10.1016/j.molstruc.2018.08.014

Kortlever, R., Shen, J., Schouten, K. J. P., Calle-Vallejo, F., and Koper, M. T. M. (2015). Catalysts and reaction pathways for the electrochemical reduction of carbon dioxide. *J. Phys. Chem. Lett.* 6, 4073–4082. doi:10.1021/acs.jpclett.5b01559

Kuhl, K. P., Cave, E. R., Abram, D. N., and Jaramillo, T. F. (2012). New insights into the electrochemical reduction of carbon dioxide on metallic copper surfaces. *Energy Environ. Sci.* 5, 7050. doi:10.1039/c2ee21234j

Landaeta, E., Masitas, R. A., Clarke, T. B., Rafacz, S., Nelson, D. A., Isaacs, M., et al. (2020). Copper-oxide-coated silver nanodendrites for photoelectrocatalytic CO2 reduction to acetate at low overpotential. *ACS Appl. Nano Mater* 3, 3478–3486. doi:10.1021/acsanm.0c00210

Landaeta, E., Schultz, Z. D., Burgos, A., Schrebler, R., and Isaacs, M. (2018). Enhanced photostability of cuprous oxide by lignin films on glassy carbon electrodes in the transformation of carbon dioxide. *Green Chem.* 20, 2356–2364. doi:10.1039/C8GC00365C

Lau, G. P. S., Schreier, M., Vasilyev, D., Scopelliti, R., Grätzel, M., and Dyson, P. J. (2016). New insights into the role of imidazolium-based promoters for the electroreduction of CO2 on a silver electrode. *J. Am. Chem. Soc.* 138, 7820–7823. doi:10.1021/jacs.6b03366

Lee, Y., Choi, J. R., Lee, K. J., Stott, N. E., and Kim, D. (2008). Large-scale synthesis of copper nanoparticles by chemically controlled reduction for applications of inkjet-printed electronics. *Nanotechnology* 19, 415604. doi:10.1088/0957-4484/19/41/415604

Leisner, C. P. (2020). Review: climate change impacts on food security-focus on perennial cropping systems and nutritional value. *Plant Sci.* 293, 110412. doi:10.1016/j.plantsci.2020.110412

Li, D., Yang, J., Qi, W., and Gao, Q. (2021). Tetrahedral CuZnInSe3 nanocrystals: one-pot synthesis, properties, and solar cell application. *J. Alloys Compd.* 854, 157096. doi:10.1016/j.jallcom.2020.157096

Li, G., Liu, H., Yang, H., Chen, X., Ji, K., Yang, D., et al. (2022a). Tuning product distributions of CO2 electroreduction over copper foil through cathodic corrosion. *Chem. Eng. Sci.* 263, 118142. doi:10.1016/j.ces.2022.118142

Li, X., Wang, J., Lv, X., Yang, Y., Xu, Y., Liu, Q., et al. (2022b). Hetero-interfaces on Cu electrode for enhanced electrochemical conversion of CO2 to multi-carbon products. *Nanomicro Lett.* 14, 134. doi:10.1007/s40820-022-00879-5

Li, Y., Li, F., Laaksonen, A., Wang, C., Cobden, P., Boden, P., et al. (2023). Electrochemical CO2 reduction with ionic liquids: review and evaluation. *Ind. Chem. Mater* 1, 410–430. doi:10.1039/D2IM00055E

Low, Q. H., Loo, N. W. X., Calle-Vallejo, F., and Yeo, B. S. (2019). Enhanced electroreduction of carbon dioxide to methanol using zinc dendrites pulse-deposited on silver foam. *Angew. Chem. - Int. Ed.* 58, 2256–2260. doi:10.1002/anie.201810991

Lu, B. J., Li, J. R., Tai, H. C., Cai, W., Tseng, H. H., and Hsieh, Y. T. (2019). A facile ionic-liquid pretreatment method for the examination of archaeological wood by scanning electron microscopy. *Sci. Rep.* 9, 13253. doi:10.1038/s41598-019-49773-y

Lu, C., Sun, Y., Liu, J., Wang, X., Liu, S. L., and Feng, W. (2015). Enhanced photochromism of heteropolyacid/polyvinylpyrolidone composite film by TiO2 doping. *J. Appl. Polym. Sci.* 132, 1–6. doi:10.1002/app.41583

Lv, Z., Shi, Y., Zang, S., and Sun, L. (2020). Spatial and temporal variations of atmospheric CO2 concentration in China and its influencing factors. *Atmos. (Basel)* 11, 231–249. doi:10.3390/atmos11030231

Ma, X., Xing, L., Liu, K., and Liu, L. (2022). Effects of electrolytes on the electrochemical reduction of CO2 to C2H4: a mechanistic point of view. *Catal. Sci. Technol.* 13, 788–801. doi:10.1039/d2cy01882a

Maniam, K. K., and Paul, S. (2021). Ionic liquids and deep eutectic solvents for CO2 conversion technologies—a review. *Materials* 14, 4519. doi:10.3390/ma14164519

Mardones-Herrera, E., Castro-Castillo, C., Nanda, K. K., Veloso, N., Leyton, F., Martínez, F., et al. (2022). Reduced graphene oxide overlayer on copper nanocube electrodes steers the selectivity towards ethanol in electrochemical reduction of carbon dioxide. *ChemElectroChem* 9, e202200259. doi:10.1002/celc.202200259

Martínez-Rojas, F., Diculescu, V. C., and Armijo, F. (2020). Electrochemical immunosensing platform for the determination of the 20S proteasome using an aminophenylboronic/poly-indole-6-carboxylic acid-modified electrode. *ACS Appl. Bio Mater* 3, 4941–4948. doi:10.1021/acsabm.0c00478

Montoya, J. H., Peterson, A. A., and Nørskov, J. K. (2013). Insights into C-C coupling in CO2 electroreduction on copper electrodes. *ChemCatChem* 5, 737–742. doi:10.1002/cctc.201200564

Montoya, J. H., Shi, C., Chan, K., and Nørskov, J. K. (2015). Theoretical insights into a CO dimerization mechanism in CO2 electroreduction. *J. Phys. Chem. Lett.* 6, 2032–2037. doi:10.1021/acs.jpclett.5b00722

Muldoon, M. J., Aki, S. N. V. K., Anderson, J. L., Dixon, J. K., and Brennecke, J. F. (2007). Improving carbon dioxide solubility in ionic liquids. *J. Phys. Chem. B* 111, 9001–9009. doi:10.1021/jp071897q

National Oceanic and Atmospheric Administration (NOAA) (n.d). Available at: https://www.noaa.gov/(Accessed February 17, 2020).

Nguyen, T. P., Nguyen, D. L. T., Nguyen, V. H., Le, T. H., Vo, D. V. N., Trinh, Q. T., et al. (2020). Recent advances in tio2-based photocatalysts for reduction of co2 to fuels. *Nanomaterials* 10, 337–361. doi:10.3390/nano10020337

Nie, X., Esopi, M. R., Janik, M. J., and Asthagiri, A. (2013). Selectivity of CO2 reduction on copper electrodes: the role of the kinetics of elementary steps. *Angew. Chem. Int. Ed.* 52, 2459–2462. doi:10.1002/anie.201208320

Noack, K., Schulz, P. S., Paape, N., Kiefer, J., Wasserscheid, P., and Leipertz, A. (2010). The role of the C2 position in interionic interactions of imidazolium based ionic liquids: a vibrational and NMR spectroscopic study. *Phys. Chem. Chem. Phys.* 12, 14153–14161. doi:10.1039/c0cp00486c

Parada, W. A., Vasilyev, D. V., Mayrhofer, K. J. J., and Katsounaros, I. (2022). CO2Electroreduction on silver foams modified by ionic liquids with different cation side chain length. *ACS Appl. Mater Interfaces* 14, 14193–14201. doi:10.1021/acsami.1c24386

Pereiro, A. B., Tomé, L. C., Martinho, S., Rebelo, L. P. N., and Marrucho, I. M. (2013). Gas permeation properties of fluorinated ionic liquids. *Ind. Eng. Chem. Res.* 52, 4994–5001. doi:10.1021/ie4002469

Polani, S., Kanovsky, N., and Zitoun, D. (2018). Leveraging commercial silver inks as oxidation reduction reaction catalysts in alkaline medium. *ACS Appl. Nano Mater* 1, 3075–3079. doi:10.1021/acsanm.8b00714

Quezada, D., Honores, J., Aguirre, M. J., and Isaacs, M. (2014a). Electrocatalytic reduction of carbon dioxide on conducting glass electrode modified with polymeric porphyrin films containing transition metals in ionic liquid medium. *J. Coord. Chem.* 67, 4090–4100. doi:10.1080/00958972.2014.974581

Quezada, D., Honores, J., García, M., Armijo, F., and Isaacs, M. (2014b). Electrocatalytic reduction of carbon dioxide on a cobalt tetrakis(4-aminophenyl) porphyrin modified electrode in BMImBF4. *New J. Chem.* 38, 3606–3612. doi:10.1039/c4nj00519h

Rosen, B. A., Salehi-Khojin, A., Thorson, M. R., Zhu, W., Whipple, D. T., Kenis, P. J. A., et al. (2011). Ionic liquid-mediated selective conversion of CO2 to CO at low overpotentials. *Science* 334, 643–644. doi:10.1126/science.1209786

Rutkowska, I. A., Wadas, A., Szaniawska, E., Chmielnicka, A., Zlotorowicz, A., and Kulesza, P. J. (2020). Elucidation of activity of copper and copper oxide nanomaterials for electrocatalytic and photoelectrochemical reduction of carbon dioxide. *Curr. Opin. Electrochem* 23, 131–138. doi:10.1016/j.coelec.2020.05.014

Schrader, B. (1996). Infrared and Raman spectroscopy. *Method Appl.* doi:10.1016/0924-2031(00)00065-5

Shahi, A. K., Pandey, B. K., Singh, B. P., Gupta, B. K., Singh, S., and Gopal, R. (2017). Photo physical studies of PVP arrested ZnS quantum dots. *Electron. Mater. Lett.* 13, 160–167. doi:10.1007/s13391-017-6132-7

Shirley, R. (2020). The CRYSFIRE system for automatic powder indexing.

Shukla, J. B., Verma, M., and Misra, A. K. (2017). Effect of global warming on sea level rise: a modeling study. *Ecol. Complex.* 32, 99–110. doi:10.1016/j.ecocom.2017.10.007

Snyder, J., Fujita, T., Chen, M. W., and Erlebacher, J. (2010). Oxygen reduction in nanoporous metal-ionic liquid composite electrocatalysts. *Nat. Mater* 9, 904–907. doi:10.1038/nmat2878

Tam, S. K., Fung, K. Y., Hang Poon, G. S., and Ng, K. M. (2016). Product design: metal nanoparticle-based conductive inkjet inks. *Am. Inst. Chem. Eng.* 62, 2740–2753. doi:10.1002/aic.15271

Tian, Y., Yu, Z., Cao, L., Zhang, X. L., Sun, C., and Wang, D. W. (2021). Graphene oxide: an emerging electromaterial for energy storage and conversion. *J. Energy Chem.* 55, 323–344. doi:10.1016/j.jechem.2020.07.006

Venezia, E., Viviani, M., Presto, S., Kumar, V., and Tomov, R. I. (2019). Inkjet printing functionalization of SOFC LSCF cathodes. *Nanomaterials* 9, 654–670. doi:10.3390/nano9040654

Wang, Q., Gao, Y., Ma, Z., Zhang, Y., Ni, W., Younus, H. A., et al. (2021). Supported ionic liquid phase-boosted highly active and durable electrocatalysts towards hydrogen evolution reaction in acidic electrolyte. *J. Energy Chem.* 54, 342–351. doi:10.1016/j.jechem.2020.06.012

Wang, S., Kou, T., Baker, S. E., Duoss, E. B., and Li, Y. (2020). Recent progress in electrochemical reduction of CO2 by oxide-derived copper catalysts. *Mater Today Nano* 12, 100096. doi:10.1016/j.mtnano.2020.100096

Wang, W., Ning, H., Fei, X., Wang, X., Ma, Z., Jiao, Z., et al. (2023). Trace ionic liquid-assisted orientational growth of Cu2O (110) facets promote CO2 electroreduction to C2 products. *ChemSusChem* 16, e202300418. doi:10.1002/cssc.202300418

World Meteorological Organization (WMO) (2019) *WMO greenhouse gas bulletin (GHG bulletin) - No. 15*, 8. Wmo. Available at: https://library.wmo.int/records/item/58687-no-15-25-november-2019?offset=5.

Wu, W., Takahashi, K., Zhou, L., and Jin, S. (2020). Income inequality and the distributional effects of elevated carbon dioxide on dietary nutrient deficiency. *J. Clean. Prod.* 265, 121606. doi:10.1016/j.jclepro.2020.121606

Xu, T., Waehler, T., Vecchietti, J., Bonivardi, A., Bauer, T., Schwegler, J., et al. (2017). Interaction of ester-functionalized ionic liquids with atomically-defined cobalt oxides surfaces: adsorption, reaction and thermal stability. *ChemPhysChem* 18, 3443–3453. doi:10.1002/cphc.201700843

Yan, Y., Bender, M. L., Brook, E. J., Clifford, H. M., Kemeny, P. C., Kurbatov, A. V., et al. (2019). Two-million-year-old snapshots of atmospheric gases from Antarctic ice. *Nature* 574, 663–666. doi:10.1038/s41586-019-1692-3

Yang, Y., Louisia, S., Yu, S., Jin, J., Roh, I., Chen, C., et al. (2023). Operando studies reveal active Cu nanograins for CO2 electroreduction. *Nature* 614, 262–269. doi:10.1038/s41586-022-05540-0

Yue, Y., Sun, Y., Tang, C., Liu, B., Ji, Z., Hu, A., et al. (2019). Ranking the relative CO2 electrochemical reduction activity in carbon materials. *Carbon N. Y.* 154, 108–114. doi:10.1016/j.carbon.2019.07.098

Zeng, S., Zhang, X., Bai, L., Zhang, X., Wang, H., Wang, J., et al. (2017). Ionic-liquid-based CO2 capture systems: structure, interaction and process. *Chem. Rev.* 117, 9625–9673. doi:10.1021/acs.chemrev.7b00072

Zhang, C., Qu, P., Zhou, M., Qian, L., Bai, T., Jin, J., et al. (2023a). Ionic liquids as promisingly multi-functional participants for electrocatalyst of water splitting: a review. *Molecules* 28, 3051. doi:10.3390/molecules28073051

Zhang, G. R., and Etzold, B. J. M. (2021). Emerging applications of solid catalysts with ionic liquid layer concept in electrocatalysis. *Adv. Funct. Mater* 31. doi:10.1002/adfm.202010977

Zhang, G.-R., Straub, S.-D., Shen, L.-L., Hermans, Y., Schmatz, P., Reichert, A. M., et al. (2020). Probing CO2 reduction pathways for copper catalysis using an ionic liquid as a chemical trapping agent. *Angew. Chem. Int. Ed.* 59, 18095–18102. doi:10.1002/anie.202009498

Zhang, M., Wu, T. S., Hong, S., Fan, Q., Soo, Y. L., Masa, J., et al. (2019). Efficient electrochemical reduction of CO2 by Ni-N catalysts with tunable performance. *ACS Sustain Chem. Eng.* 7, 15030–15035. doi:10.1021/acssuschemeng.9b03502

Zhang, X., Liu, Z., and Wang, W. (2008). Screening of ionic liquids to capture CO2 by COSMO-RS and experiments. *AIChE J.* 54, 2717–2728. doi:10.1002/aic.11573

Zhang, Y., Qiu, W., Liu, Y., Wang, K., Zou, L., Zhou, Y., et al. (2023b). Hydrophobic surface efficiently boosting Cu2O nanowires photoelectrochemical CO2 reduction activity. *Chem. Commun.* 59, 5914–5917. doi:10.1039/d3cc00825h

Zhou, B., Kong, X., Vanka, S., Cheng, S., Pant, N., Chu, S., et al. (2019). A GaN:Sn nanoarchitecture integrated on a silicon platform for converting CO2 to HCOOH by photoelectrocatalysis. *Energy Environ. Sci.* 12, 2842–2848. doi:10.1039/c9ee01339c

Zhou, F., Liu, S., Yang, B., Wang, P., Alshammari, A. S., and Deng, Y. (2014). Highly selective electrocatalytic reduction of carbon dioxide to carbon monoxide on silver electrode with aqueous ionic liquids. *Electrochem Commun.* 46, 103–106. doi:10.1016/j.elecom.2014.06.023